4

Solid State Research

1970

Prepared under Electronic Systems Division Contract F19628-70-C-0230 by

Lincoln Laboratory
MASSACHUSETTS INSTITUTE OF TECHNOLOGY
Lexington, Massachusetts

ESD-TR-70-350

MASSACHUSETTS INSTITUTE OF TECHNOLOGY
LINCOLN LABORATORY

5 March 1971

TO ALL HOLDERS OF SOLID STATE RESEARCH REPORT (1970:4):

Please substitute the attached page for the printed page 25 of the report.

Publications Office
Lincoln Laboratory
P. O. Box 73
Lexington 73, Massachusetts

Enc. (1)

4

Solid State Research

1970

Issued 9 February 1971

Prepared under Electronic Systems Division Contract F19628-70-C-0230 by

Lincoln Laboratory

MASSACHUSETTS INSTITUTE OF TECHNOLOGY

Lexington, Massachusetts

The work reported in this document was performed at Lincoln Laboratory, a center for research operated by Massachusetts Institute of Technology, with the support of the Department of the Air Force under Contract F19628-70-C-0230.

ABSTRACT

This report covers in detail the solid state research work of the Solid State Division at Lincoln Laboratory for the period 1 August through 31 October 1970. The topics covered are Solid State Device Research, Materials Research, Physics of Solids, and Microelectronics. The Microsound work is sponsored by ABMDA and is reported under that program.

Accepted for the Air Force
Joseph R. Waterman, Lt. Col., USAF
Chief, Lincoln Laboratory Project Office

INTRODUCTION

I. SOLID STATE DEVICE RESEARCH

Hall coefficient and electrical resistivity measurements were carried out on $Hg_{1-x}Cd_xTe$ single crystal specimens obtained from a high quality, highly homogeneous crystal grown by the new method described in the previous report.

The responsivity of GaAs extrinsic far infrared detectors has been studied under low background conditions using a calibrated GaAs far infrared spontaneous emitter as a source and a cold blackbody to provide the background. The observed variation in responsivity with blackbody temperature from 10° to 300°K correlates with the observed variation in sample impedance.

Lifetime measurements of the extrinsic photoconductivity response of GaAs to radiation at 337 μ (and in one case also at 195 μ) have been obtained in the range between 25 and 250 nsec for samples with different donor and acceptor concentrations. In general, samples with higher acceptor concentrations have shorter lifetimes, as expected.

Photoluminescence lines involving exciton-neutral donor complexes in high purity GaAs have been identified using a magnetic field. Two sets of five lines each are identified: a higher energy set including free exciton recombination, exciton recombination at a neutral donor and exciton recombination at three complex centers all involving a neutral donor, and a replica of this set of five lines at lower energy consisting of the same transitions with the neutral donor left in a terminal excited (n = 2) state.

The first CW operation of a Raman laser has been achieved using a liquid nitrogen cooled CO laser and the spin-flip scattering from conduction electrons in InSb in a magnetic field. CO laser pump threshold powers as low as 200 mW have been observed, and CW output powers between 0.5 and 1 W have been obtained with tuning between 5.65 and 5.88 μ for a maximum 50-kG field.

High speed $Hg_{1-x}Cd_xTe$ photodiodes have been fabricated which at 77°K have quantum efficiencies of 20% and detectivities of 3×10^9 cmHz$^{1/2}$/Watt at 10.6 μ. The 3 dB point occurs at about 500 MHz; however, a substantial signal is observed to the limit of the measurements at 1.2 GHz.

II. MATERIALS RESEARCH

The total vapor pressure over molten Bi_2Te_3 has been measured between 707° and 896°C by means of a new manometric technique. Comparison of the results with those obtained by measuring the optical density of the vapor shows that $Bi_2Te_3(\ell)$ does not vaporize congruently, since the vapor contains at least 95 atomic percent Te over the entire temperature range investigated.

Three high-pressure polytypes of $RbFeCl_3$ have been prepared at pressures between 15 and 35 kbars and then retained at atmospheric pressure. One polytype, which has the same structure as the atmospheric pressure form of $RbNiF_3$, is a ferrimagnet with Curie point of 109°K and is transparent between 0.3 and 24μm, except for some absorption bands between 0.3 and 0.7μm.

A review of high-pressure synthesis, as illustrated by studies on compounds with the chemical formula ABX_3 or $(AX_n)(ABX_3)$, where A and B are cations and X is an anion, has been prepared for publication as a chapter in Preparative Methods in Solid State Chemistry.

The volume compression of cubic TiO_x, with x = 0.85, 1.0, 1.11 and 1.25, has been determined by x-ray diffraction measurements of the lattice parameter as a function of pressure. For the first two compositions, the volume compression is independent of pressure up to 140 kbars. For the two oxygen-rich compositions, the relatively large initial compression decreases with increasing pressure until it becomes essentially constant above 20 kbars.

III. PHYSICS OF SOLIDS

Shubnikov-deHaas measurements have been carried out in $Pb_{1-x}Sn_xSe$, with x = 0.08, 0.17 and 0.20. The results indicate pockets of holes and electrons at the L-point of the Brillouin zone and, if one assumes mirror bands, that a six-band model gives better agreement than a two-band model.

Ultrasonic attenuation experiments in the frequency range 20 to 200 MHz have been initiated in order to explore the Fermi surface of holes in bismuth, which was recently reported to have a saddle point. No nonextremal Fermi surface cross sections are observed, even for the sound wave vector nearly perpendicular to the magnetic field.

High resolution, far-infrared laser studies of hydrogenic donors in GaAs have been extended to higher magnetic fields, different transitions and additional samples. At the high fields, the central cell correction varies with magnetic field, since the wave function in the immediate vicinity of the impurity varies with field; using perturbation theory, quantitative agreement is obtained with a calculation based on effective mass wave functions.

A description of a smooth semiconductor-metal transition has been obtained, including both electron-electron Coulomb energy and lattice displacement energy. For Ti_2O_3, a calculation based on lattice displacement energy as dominant leads to reasonable qualitative agreement with experiment.

A procedure has been formulated for calculating the first few moments of the frequency dependent conductivity of a narrow band material in the Hubbard model. A method is proposed for using these moments to identify a Mott transition.

A relaxation time Ansatz has been established which treats both orbital and spin relaxation consistently in quantum transport theory. This approach conserves charge and spin

density, and is important intreating such phenomena as spin-flip Raman scattering. This relaxation time Ansatz has also been incorporated into a calculation of the spectra of inelastic light scattering from acoustic plasma waves and single particle excitations in a semiconductor plasma in a magnetic field. The calculation indicates that the acoustic wave light scattering should be detectable with currently availahle experimental techniques.

Rushbrooke and Wood, and Domb and Sykes have contended on the basis of high-temperature power-series expansions that the standard procedure for determining experimentally the paramagnetic Curie temperatures, by extrapolating the (apparently) linear portion of the $1/\chi$ versus T curve back to the temperature axis, is significantly in error. This has been examined in detail for EuO and $CdCr_2S_4$. The model-independent high-temperature power-series expansion is fit to experimental data, and from this fit true asymptotes are computed; these asymptotes are shown to be quite different from those obtained by the standard extrapolation procedure.

A finite temperature graphical theory for two-magnon scattering in a simple antiferromagnet has been constructed. The theory at $T = 0°K$ leads to the familiar result using two-time Green's functions and the Tyablikov decoupling scheme. Finite temperature calculations are under way.

A study of Raman scattering of argon ion laser radiation in the transparent antiferromagnet FeF_2 has revealed, in addition to the Raman-active phonon and magnon excitations previously reported in the energy range below 500 cm^{-1}, a new series of lines shifted approximately 1100 cm^{-1} from the laser. The temperature dependence of this new series suggests some relation to magnetic ordering, although a detailed identification has not yet been made.

With the use of a simple theoretical model consisting of a one-dimensional slab of cold nonuniform plasma immersed in a uniform magnetic field, harmonic generation has been studied. This model, which has been previously proven capable of explaining qualitatively both CW linear response and nonlinear echo experiments, predicts (1) strong odd harmonic generation compared to even harmonic generation, and (2) for small collision frequencies, strongest odd harmonic generation occurring near cyclotron and upper hybrid resonances.

IV. MICROELECTRONICS

The semiconductor area is operational and several components have heen delivered, including photodiode arrays, E-Bird devices, gallium arsenide Schottky barrier millimeter wave diodes, and surface wave amplifier silicon substrates.

The environmental test area useful in insuring that no fundamental faults exist in the hybrid or monolithic prototype integrated circuits is now operational. In addition to complete environmental tests of all fabricated units, sample lots are tested for long-term degradation.

Considerable effort is being made to institute inspection and process control procedures to insure the continued quality of existing processes and techniques and to improve the yield and quality of some presently unsatisfactory or low yield process steps.

Introduction

The laser scanning system for monolithic integrated circuit testing continues to show promise and is presently heing implemented in our inspection and testing of integrated circuit chips. The design and construction of a faster scan for transient analysis as well as for gain measurements are in progress.

An empirically derived relationship, which predicts the total substrate area required for an integrated circuit layout based on component area and total number of internal and external connections, is under study and currently has sufficient accuracy to be helpful in reducing or eliminating trial layouts. A computer program to make use of the predicted area, yield and cost relationship of different interconnecting line widths and process variables is in the planning stages. The empirical relationship derived is finding use in printed circuit layouts and monolithic structures, as well as in hybrid integrated circuits.

CONTENTS

ORGANIZATION

SOLID STATE DIVISION

A. L. McWhorter, *Head*
P. E. Tannenwald, *Associate Head*
C. R. Grant, *Assistant*

SOLID STATE THEORY

H. J. Zeiger, *Leader*
M. M. Litvak, *Assistant Leader*

Bari, R. A.
Brine, N. S.
Brodersen, R. W.*
Davies, R. W.
Dresselhaus, G. F.
Landon, S. N.
Larsen, D. M.
Ngai, K. L.
Palm, B. J.†
Young, C. Y.

ELECTRONIC MATERIALS

J. B. Goodenough, *Leader*
A. J. Strauss, *Associate Leader*

Anderson, C. H., Jr.
Banus, M. D.
Batson, D. A.
Button, M. J.
Capes, R. N., Jr.
Delaney, E. J.
England, R. E.
Fahey, R. E.
Finn, M. C.
Iseler, G. W.
Kafalas, J. A.
LaFleur, W. J.
Lavine, M. C.†
Leyenaar, A. R.
Longo, J. M.
Mastromattei, E. L.
Mroczkowski, I. H.
Owens, E. B.
Pantano, J. V.
Pierce, J. W.
Plonko, M. C.
Raccah, P. M.
Reed, T. B.
Roddy, J. T.
Smith, F. T. J.
Stack, T. E.
Steininger, J. M.
Temkin, R. J.*
Tracy, D. M.

MICROELECTRONICS

R. E. McMahon, *Leader*

Bachner, F. J.
Beatrice, P. A.
Childs, N. B.
Clough, T. F.
Cohen, R. A.
Durant, G. L.
Grant, L. L.
Gray, R. V.
McBride, W. F.
McGonagle, W. H.
Mountain, R. W.
Pichler, H. H.
Pybus, V. J.
Wilde, R. E.

SOLID STATE PHYSICS

J. G. Mavroides, *Leader*
G. B. Wright, *Assistant Leader*

Allen, J. W.
Barch, W. E.
Blum, F. A., Jr.
Brandt, R. C.
Burke, J. W.
Chinn, S. R.
DeFeo, W. E.
Dresselhaus, M. S.†
Dwight, K., Jr.
Feldman, B.
Fetterman, H.
Groves, S. H.
Henrich, V. E.
Johnson, E. J.
Kernan, W. C.
Kolesar, D. F.
McIngailis, J.
Menyuk, N.
Nill, K. W.
Parker, C. D.
Pine, A. S.
Weber, R.

APPLIED PHYSICS

J. O. Dimmock, *Leader*
T. C. Harman, *Assistant Leader*
I. Melngailis, *Assistant Leader*

Belanger, L. J.
Brueck, S. R. J.*
Calawa, A. R.
Carter, F. B.
Caswell, F. H.
DeMeo, N.
Donnelly, J. P.
Elliott, C. T.‡
Ferrante, G. A.
Foyt, A. G.
Hancock, R.
Hurwitz, C. E.
Krohn, L., Jr.
Lindley, W. T.
Mooradian, A.
Murphy, R. A.*
Orphanos, W. G.
Paladino, A. E.
Rossi, J. A.
Spears, D. L.
Stillman, G. E.
Ward, J. H. R., III
Wolfe, C. M.
Woods, R. J.
Youtz, P.

MICROSOUND

E. Stern, *Leader*

Alusow, J. A.
Brogan, W. T.
Burke, B. E.
Chen, F.
Smith, H. I.
Waldron, R. A.
Williamson, R.

---

* Research Assistant
† Part Time
‡ Exchange Scientist, RRE

REPORTS BY AUTHORS ENGAGED IN SOLID STATE RESEARCH

15 August through 15 November 1970

PUBLISHED REPORTS

Journal Articles*

JA No.			
3320	Single Crystal Lead-Tin Chalcogenides	I. Melngailis T. C. Harman	Chapter 4 in Semiconductors and Semimetals (Academic Press, New York, 1970), p. 111
3539	Positron Annihilation in Copper – Comparisons of Different Results	J. Melngailis	Phys. Rev. B 2, 563 (1970)
3546	Transport Equation for a Fermi System in Random Scattering Centers. II. Independent Electrons in an Arbitrarily Varying Electric Field and Strong Single-Center Potentials	J. L. Sigel P. N. Argyres†	Phys. Rev. B 1, 1845 (1970), DDC AD-709758
3587	Split-Off Valence Band Parameters for GaAs from Stress-Modulated Magnetoreflectivity	M. Reine† R. L. Aggarwal† B. Lax† C. M. Wolfe	Phys. Rev. B 2, 458 (1970)
3608	Vapor-Crystal Equilibrium and Electrical Properties of HgTe	A. J. Strauss R. F. Brebrick	J. Phys. Chem. Solids 31, 2293 (1970)
3618	Phase Diagram of the Zn-Cd-Te Ternary System	J. Steininger A. J. Strauss R. F. Brebrick	J. Electrochem. Soc. 117, 1305 (1970)
3620	Interband Magnetoreflection of α-Sn	S. H. Groves C. R. Pidgeon† A. W. Ewald† R. J. Wagner†	J. Phys. Chem. Solids 31, 2031 (1970)
3663	Crystal Structure of Hexagonal $RbNiF_3$(6H)	R. J. Arnott† J. M. Longo	J. Solid State Chem. 2, 416 (1970)
3678A	Rigid and Nonrigid Beam Lead Substrates	F. J. Bachner R. A. Cohen R. E. McMahon	Solid State Tech. 13, 62 (1970)
3686	Polarized Maser Emission from Interstellar OH and H_2O	M. M. Litvak	Phys. Rev. A 2, 937 (1970)

* Reprints available.

† Author not at Lincoln Laboratory.

JA No.			
3687	Phase Diagram of the CdTe-CdSe Pseudobinary System	A. J. Strauss J. Steininger	J. Electrochem Soc. 117, 1420 (1970)
3691	Phase Transitions in Perovskite-like Compounds of the Rare Earths	S. Geller* P. M. Raccah	Phys. Rev. B 2, 1167 (1970)
3712	Translational Symmetry and Orbital Anisotropic Exchange in Cr_2O_3	J. W. Allen	Phys. Rev. Letters 25, 934 (1970)
3716	Phase Diagram of the PbTe-PbSe Pseudobinary System	J. Steininger	Metallurgical Trans. 1, 2939 (1970)
3721	Seebeck Coefficients in Vanadium Spinels	J. B. Goodenough	Mat. Res. Bull. 5, 621 (1970)
3749	Acoustic Surface Wave Amplification Using an Accumulation Layer on Silicon	B. E. Burke A. Bers* H. I. Smith R. A. Cohen R. W. Mountain	Proc. IEEE 58, 1775-1776 (October 1970)
MS-2681	Optical Reflectance Study of Magnetic Ordering Effects in EuO, EuS, EuSe and EuTe	C. R. Pidgeon* J. Feinleib W. J. Scouler J. O. Dimmock T. B. Reed	IBM J. Res. Dev. 14, 309 (1970)

* * * * *

UNPUBLISHED REPORTS

Journal Articles

JA No.			
3627	Polarons Bound in a Coulomb Potential. II. 2P State Zeeman Effect	D. M. Larsen	Accepted by Phys. Rev.
3661	Collective Oscillations in a Simple Metal. I. Spin Waves	A. R. Wilson D. E. Fredkin*	Accepted by Phys. Rev. B
3725	Harmonic Generation in Cold Non-uniform Plasma in a Magnetic Field	F. A. Blum	Accepted by Phys. Fluids
3735	High Pressure Synthesis	J. B. Goodenough J. A. Kafalas J. M. Longo	Accepted as chapter in Preparative Methods in Solid State Chemistry (Academic Press, New York)

* Author not at Lincoln Laboratory.

JA No.			
3740	Resonant Coupling of Landau Levels via LO Phonons in Polar Semiconductors and Its Effect on the Landau Level Raman Scattering from Semiconductor Plasmas	K. L. Ngai	Accepted by Phys. Rev.
3748	Shubnikov-deHaas Measurements in $Pb_{1-x}Sn_xTe$	J. Melngailis T. C. Harman J. G. Mavroides J. O. Dimmock	Accepted by Phys. Rev.
3751	Composition Stability Limits for the Rocksalt-Structure Phase $(Pb_{1-y}Sn_y)_{1-x}Te_x$ from Lattice Parameter Measurements	R. F. Brebrick	Accepted by J. Phys. Chem. Solids
3761	Conceptual Phase Diagram and Its Application to the Spontaneous Magnetism of Several Pyrites	J. B. Goodenough	Accepted by J. Solid State Chem.
3765	Raman Scattering in $CsMnF_3$	S. R. Chinn	Accepted by Phys. Rev.
3767	The Structure of the High and Low Pressure Forms of $SrIrO_3$	J. M. Longo J. A. Kafalas R. J. Arnott*	Accepted by J. Solid State Chem.
3772	Polaron Zeeman Effect of Shallow Donors in CdTe	D. R. Cohn* D. M. Larsen B. Lax*	Accepted by Solid State Commun.
3773	Even Parity Levels of Donors in Si	W. H. Kleiner W. E. Krag	Accepted by Phys. Rev. Letters
3777	Perturbation Theory for the Bound Polaron	D. M. Larsen	Accepted by J. Phys. Chem. Solids
3789	Identification of Exciton-Neutral Donor Complexes in the Photoluminescence of High Purity GaAs	J. A. Rossi C. M. Wolfe G. E. Stillman J. O. Dimmock	Accepted by Solid State Commun.
3795	The Fermi Surface and Optical Properties of Potassium	G. Dresselhaus A. Wilson C-Y. Young	Accepted by Solid State Commun.
3796	Acceptor Luminescence in High Purity n-Type GaAs	J. A. Rossi C. M. Wolfe J. O. Dimmock	Accepted by Phys. Rev. Letters
3799	Continuous Stimulated Spin-Flip Raman Scattering in InSb	A. Mooradian S. R. J. Brueck F. A. Blum	Accepted by Appl. Phys. Letters

* Author not at Lincoln Laboratory.

JA No.			
3812	Two-Magnon Raman Scattering and Exchange Interactions in Antiferromagnetic $KNiF_3$ and K_2NiF_4 and Ferrimagnetic $RbNiF_3$	S.R. Chinn H.J. Zeiger J.R. O'Connor	Accepted by Phys. Rev. B
3814	Absence of Hartree-Fock Behavior in Simple Decoupling Solution of Correlated Narrow-Energy-Band Model	R.A. Bari T.A. Kaplan	Accepted by Phys. Letters

Meeting Speeches*

MS No.			
2528D	Light Scattering in Semiconductors	A. Mooradian	Seminar, Japan Broadcasting Corporation, Tokyo, 4 September 1970
2702A	Rigid and Nonrigid Beam Lead Substrates	R.E. McMahon R.A. Cohen F.J. Bachner	EPECON, Toronto, Canada, 28 September – 1 October 1970
2723G	Laser Raman Spectroscopy	A. Mooradian	Seminar, Worcester Polytechnic Institute, 22 October 1970
2799A	Optical Study of the Semiconductor to Metal Transition in Ti_2O_3	P.M. Raccah	Solid State Seminar, Purdue University, 10-11 November 1970
2850A	Comparison of Experimental Charge Densities with Solid-State Calculations	P.M. Raccah	
2863	Effects of Hydrostatic Pressure and of Jahn-Teller Distortions on the Magnetic Properties of $RbFeF_3$	J.B. Goodenough N. Menyuk K. Dwight J.A. Kafalas	Conférence Internationale de Magnétisme, Grenoble, France, 14-19 September 1970
2873	Detection, Generation and Mixing of Far Infrared Radiation in GaAs	P.E. Tannenwald H. Fetterman G.E. Stillman C.M. Wolfe J.O. Dimmock I. Melngailis	Sixth International Quantum Electronics Conference, Kyoto, Japan, 7-10 September 1970
2911	Light Scattering in Solids	A. Mooradian	
2877	Magneto-Optics of Polarons in Semiconductors	D.M. Larsen	Tenth International Conference on the Physics of Semiconductors, Cambridge, Massachusetts, 17-21 August 1970
2880	Excited 1s-Like Levels of Bi Donors in Si	W.E. Krag W.H. Kleiner H.J. Zeiger	

* Titles of Meeting Speeches are listed for information only. No copies are available for distribution.

MS No.			
2882	Electron and Phonon Dispersion Relations in Tellurium	G. Dresselhaus M. S. Dresselhaus	Tenth International Conference on the Physics of Semiconductors, Cambridge, Massachusetts, 17-21 August 1970
2883	Light Scattering from Plasmons in InSb	F. A. Blum A. Mooradian	
2884	Polaron Zeeman Effects in the Silver Halides	R. C. Brandt D. M. Larsen D. R. Cohn*	
2886	Interaction of Bound Electrons with Local and Resonant Modes in Semiconductors	R. W. Davies H. J. Zeiger	
2888	Role of the Crystal C/A Ratio in Ti_2O_3 and V_2O_3	J. B. Goodenough	
2892	Variational Approach to the Metal-Semiconductor Transition	T. A. Kaplan R. A. Bari	
2893	A Raman Study of the Semiconductor-Metal Transition in Ti_2O_3	A. Mooradian P. M. Raccah	
2907	Light Scattering from Hot Electrons in Semiconductors	A. Mooradian A. L. McWhorter	
2917	High-Purity GaAs	C. M. Wolfe G. E. Stillman J. A. Rossi E. B. Owens W. T. Lindley J. O. Dimmock	Third International Symposium on GaAs and Related Compounds, Aachen, Germany, 5-7 October 1970
2919	GaAs Far Infrared Detectors and Emitters	G. E. Stillman C. M. Wolfe J. O. Dimmock	
2926	Aluminum Beam Leaded Chips, Substrates and Crossovers: A Single Metal System	R. A. Cohen F. J. Bachner R. E. McMahon	Conference on Preparation and Properties of Electronic and Magnetic Materials for Computers, New York, 30 August – 2 September 1970
2937	Effect of Pressure on the Structure and Properties of ABX_3 Compounds	J. M. Longo	American Chemical Society Regional Meeting, Providence, R. I., 19 October 1970
2950	Excitation of Interstellar Molecules	M. M. Litvak	Fourteenth General Assembly of the International Astronomical Union, Brighton, Sussex, England, 18-27 August 1970

* Author not at Lincoln Laboratory.

Reports

MS No.			
2951	Localized versus Itinerant Electrons in Magnetic Solids	J. B. Goodenough	Summer School on Theory of Magnetism of Metals, Zakopane, Poland, 31 August – 11 September 1970
2962	A Low Power Density GaAs/$LiNbO_3$ Surface Wave Amplifier	D. L. Spears B. E. Burke	Symposium on Sonics and Ultrasonics, San Francisco, 21-23 October 1970
2964	Magneto-Optical Properties of the Europium Chalcogenides	J. O. Dimmock	Conference on the Physics of Opto-Electronic Materials, Warren, Michigan, 5-6 October 1970
2992	Varied Roles of Outer d Electrons	J. B. Goodenough	The Robert A. Welch Foundation Conferences on Chemical Research. XIV. Solid State Chemistry, Houston, Texas, 9-11 November 1970

I. SOLID STATE DEVICE RESEARCH

A. CHARACTERIZATION OF $Hg_{1-x}Cd_xTe$ CRYSTALS GROWN BY A NEW METHOD

Hall coefficient and electrical resistivity measurements were carried out on as-grown, polished and etched $Hg_{1-x}Cd_xTe$ single crystal specimens at 4° and 77°K. The specimens were obtained from a high quality, highly homogeneous, $Hg_{1-x}Cd_xTe$ crystal grown by the new method described in the previous report.[1] The results of these measurements are displayed in Figs. I-1 and I-2 as a function of position, y, along the single crystal. The variation in the mole fraction of CdTe, x, is also indicated in the figures. The composition of the first 4 mm of crystal is longitudinally uniform to within experimental error of the electron microprobe, i.e., $x = 0.179 \pm 0.003$. All specimens were homogeneous in the plane transverse to the growth direction. The highest hole mobility of 415 cm^2/V-sec at 77°K with a hole carrier concentration of $1.5 \times 10^{17}/cm^3$ occurred at y = 3 mm, which corresponds to a position approximately 3 mm from the steady state liquid-solid interface. A rather sharp discontinuity in electrical characteristics occurred between

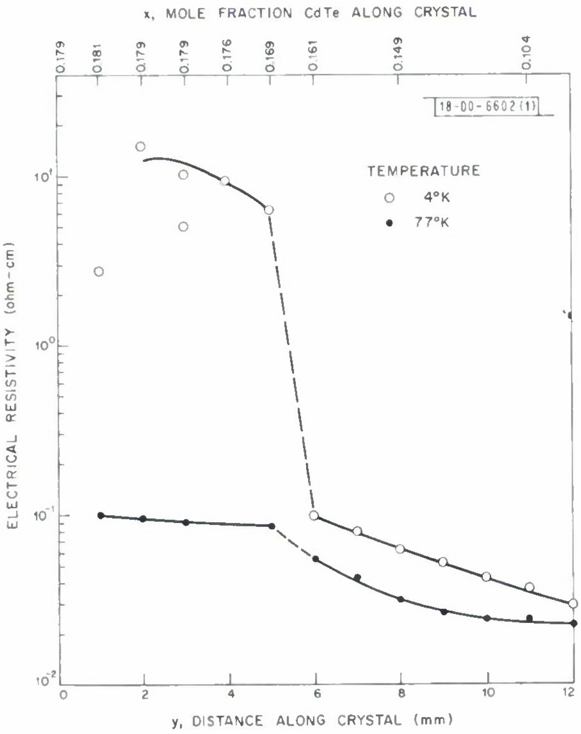

Fig. I-1. Electrical resistivity versus both the distance along the crystal, y, and the mole fraction of CdTe, x, at the temperatures of 77° and 4°K.

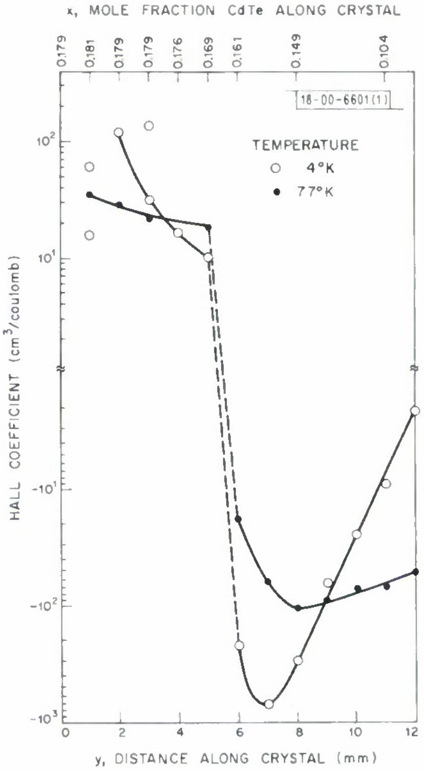

Fig. I-2. Hall coefficient versus both the distance along the crystal, y, and the mole fraction of CdTe, x, at the temperatures of 77° and 4°K.

x = 0.161 and x = 0.169, which strongly suggests that the semimetal-to-semiconductor transition occurs within this compositional range. The electrical characteristics in the y = 6 mm to y = 13 mm are consistent with a semimetal band model. The Hall coefficient measurements for material in the y = 0 to y = 5-mm region at 4°K yields values with widely varying magnitudes. This behavior is not understood at the present time.

T. C. Harman

B. GaAs FAR-INFRARED DETECTORS IN REDUCED BACKGROUND

The responsivity of GaAs far-infrared detectors[2] under low-temperature background conditions such as those encountered in rocket-borne far-infrared astronomy has been studied using a calibrated GaAs far-infrared spontaneous emitter. The arrangement used for these measurements is shown in Fig. I-3. This dewar insert permits the detector being studied to be simultaneously exposed to radiation from the emitter and to radiation from either the cold blackbody or from an external source. The rotating turret, which is positioned between the bottom end of the light pipe and the entrance to the detector cone, is used either to insert cold filters into the light path or to block the path with the conical blackbody. A vacuum-sealed crystal quartz window is used at the entrance to the detector. The chamber containing the turret can be either evacuated or backfilled with He exchange gas. In this manner the blackbody temperature can be maintained constant at any value from less than 4.2° to 300°K. A small cold preamplifier with a 37-megohm load resistor is used to reduce the effects of shunt capacitance because of the high detector resistance.

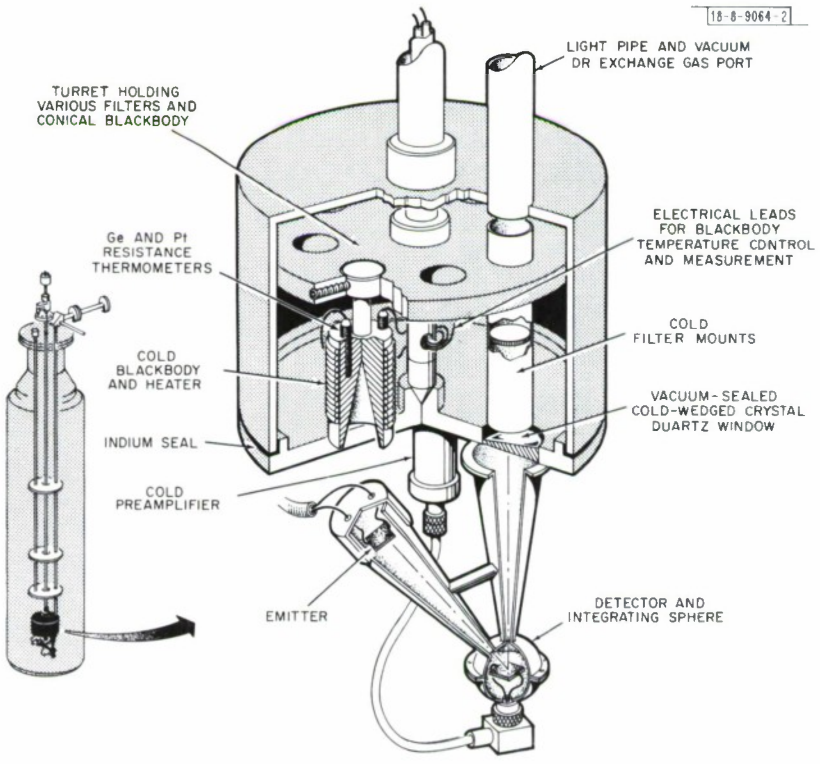

Fig. I-3. Experimental arrangement far reduced background measurements.

The detector was first calibrated using filtered, chopped radiation from an external blackbody source. The path between the external blackbody and the entrance to the light pipe was purged with dry nitrogen gas to reduce water vapor absorption. The responsivity of the detector at wave number ν can be written as $R(\nu) = R_p \cdot r(\nu)$ where R_p is the responsivity at the peak of the relative spectral sensitivity curve and $r(\nu)$ is the relative spectral sensitivity. The peak spectral responsivity is then given by

$$R_p = V(T_{BB}) \Big/ \int_0^\infty r(\nu) \cdot W(\nu, T_{BB})\, d\nu \quad ,$$

where $V(T_{BB})$ is the measured signal and $W(\nu, T_{BB})$ is the spectral flux $[W/(cm^{-1})]$ incident on the detector with the blackbody at temperature T_{BB}. This flux $W(\nu, T_{BB})$ was corrected for the transmission of filters, windows, etc., in the optical path and for emission from the chopper blade. Previous measurements have shown that, as expected, R_p is very dependent on the background radiation reaching the detector.[2] For "normal" background conditions [300°K background warm black-polyethylene (BPE) and cold crystal quartz (XQ) filters in a light pipe] the peak responsivity of this detector was determined to be $R_p = 9 \times 10^4$ V/W. For "reduced" background conditions (i.e., with filters for "normal" conditions above plus an additional cold, long wavelength pass filter which blocked most of the radiation with wavelengths shorter than 150 μ) the peak responsivity was 2.6×10^5 V/W.

The emitter was then calibrated as a function of emitter current using the calibrated detector operating under the above background conditions. The emitter current was a square-wave current pulse with a frequency of 260 Hz, and the resulting signal was synchronously detected with a lock-in voltmeter. The spectral emitter power at current I and wave number ν can be written as $\mathcal{E}(I, \nu) = \mathcal{E}_p(I) \cdot \epsilon(\nu)$, since the relative spectral distribution of the emission $\epsilon(\nu)$ does not change for the range of currents used here. The total emitted power is then

$$\mathcal{E}_T(I) = \int_0^\infty \mathcal{E}_p(I) \cdot \epsilon(\nu)\, d\nu \quad ,$$

and the peak spectral radiant intensity is

$$\mathcal{E}_p(I) = \frac{V(I, f)}{R_p \int_0^\infty r(\nu) \cdot \epsilon(\nu)\, d\nu} \quad ,$$

where $V(I, f)$ is the detector signal for the specified emitter current and frequency, and R_p is the peak spectral responsivity for the detector under the same background condition.

The results of this calibration are shown in Fig. I-4. Even though the detector responsivity varied somewhat, the day-to-day repeatability of this calibration was about ±1 percent. The detector responsivity variation was apparently caused by warming of the light pipe and an associated increase in background radiation at lower liquid helium levels. The total emitted power could be varied from about 10^{-10} to about 3×10^{-8} W for the configuration used here without evidence of heating.

The turret was then rotated so that the light pipe was blocked and the detector was exposed to the radiation from the conical blackbody. The variation of the V-I characteristics of the detector for several different blackbody temperatures as well as for the "reduced" and "normal"

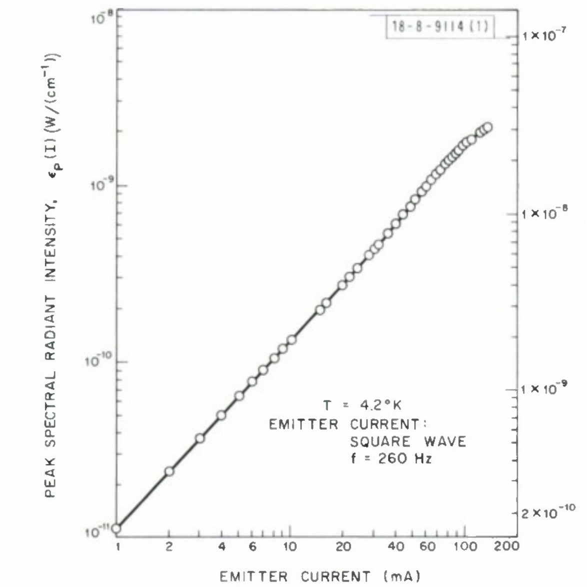

Fig. I-4. Emitter calibration curve.

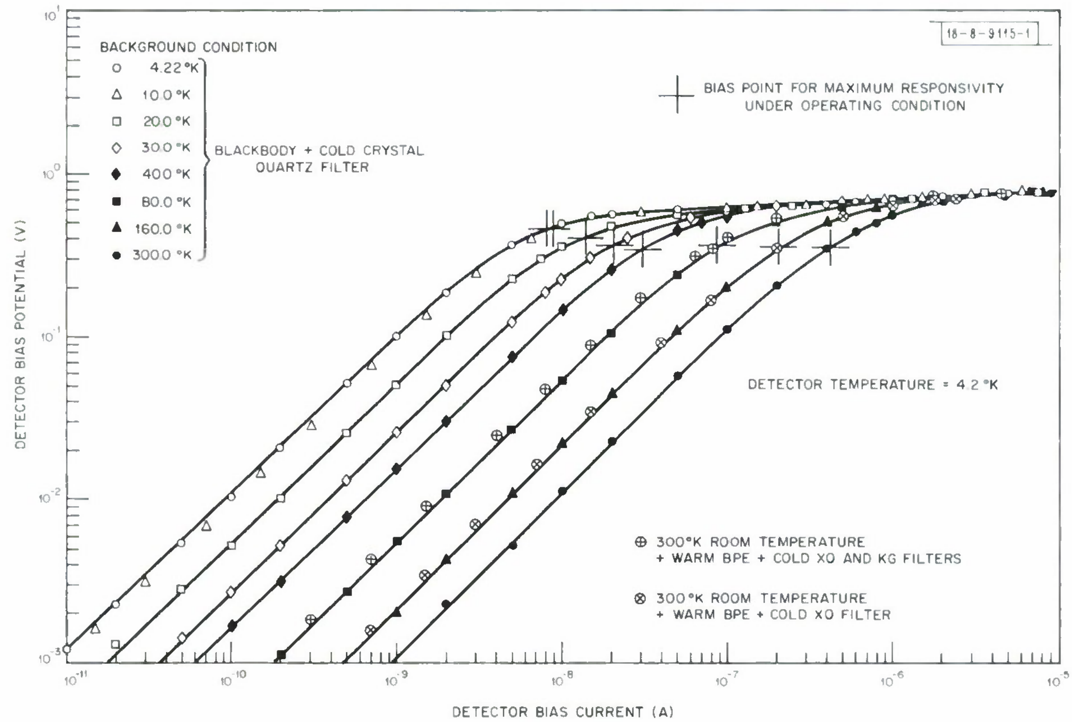

Fig. I-5. Variation of detector V-I characteristic with blackbody background temperature.

300°K background conditions mentioned earlier are shown in Fig. I-5. The curves all have essentially the same shape. They are all ohmic at low currents and voltages, and they all show the characteristic increase in conductance near the breakdown voltage which is not changed by the background radiation. For the 4.2°K background the ohmic resistance is about 1×10^8 ohms. For a 10°K background the ohmic resistance has only decreased to 9.4×10^7 ohms. This indicates that at these background levels the thermal generation of carriers from the shallow donor levels is dominant. For the 20°K blackbody background, however, the ohmic resistance has decreased to about 5.1×10^7 ohms. This indicates that for this 20°K F/2 background and a detector temperature of 4.2°K the thermal and background carrier generation rates are approximately equal. For a 300°K blackbody background the ohmic sample resistance is two orders of magnitude lower than that for the 4.2°K background. The "normal" and "reduced" 300°K background conditions correspond to blackbody backgrounds of about 160° and 80°K, respectively. The lower sample resistance for the 300°K blackbody background as compared to the normal 300°K background indicates that the cold light pipe attenuates the room temperature background by about a factor of two.

The operating points for maximum responsivity are also shown in Fig. I-5. The higher bias voltages at background temperatures below 40°K are due to loading effects of the 37-megohm load resistor. That is, at the higher bias voltages the sample resistance is lower and more closely matched to the load resistor.

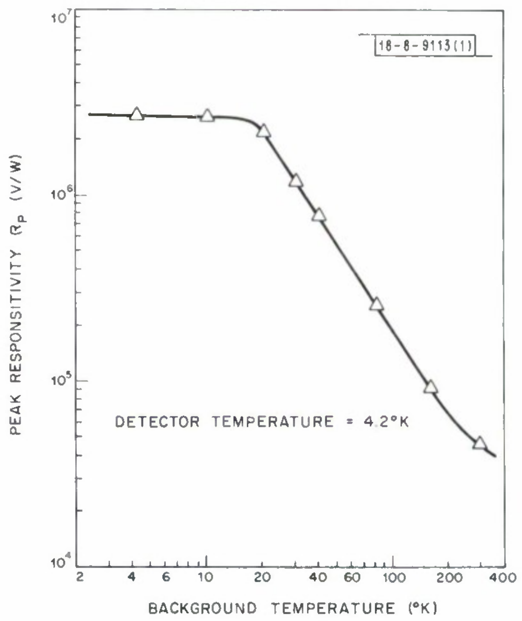

Fig. I-6. Variation of peak responsivity with blackbody background temperature.

The variation of the peak responsivity of the detector with blackbody background temperature is shown in Fig. I-6. The responsivity was determined by using the relation

$$\mathcal{R}_p(T_{BG}) = \frac{V(\mathcal{E}_I, T_{BG})}{\mathcal{E}_p(I) \int_0^\infty r(\nu) \cdot \epsilon(\nu)\, d\nu} \quad ,$$

where $R_p(T_{BG})$ is the peak detector responsivity (V/W) for the blackbody background temperature T_{BG}, and $V(\mathcal{E}_I, T_{BG})$ is the signal measured for the calibrated emitter peak spectral radiant intensity $\mathcal{E}_p(I)$.

There is little change in the responsivity for background temperatures between 4.2° and 10°K, another indication that in this background range the detector conductance is limited mainly by thermal generation of carriers. However, for background temperatures of 20°K and higher, the responsivity decreases rapidly with increasing background temperature. The signal voltage V_s for a nonohmic detector can be written as[3]

$$V_s = \frac{V(g_s/g)}{1 + g_\ell/g + \frac{V}{g}(\partial g/\partial V)_G} ,$$

where V_s is the signal voltage, V the detector DC bias voltage, g the DC detector conductance, g_ℓ the load conductance, g_s the increase in conductance due to the signal and $(\partial g/\partial V)_G$ the change in sample conductance with voltage at a constant background generation rate. The nonohmic effect and the loading effect of a finite load conductance are included in the denominator of this expression and only serve to decrease the signal voltage somewhat. The major variation of the signal with background radiation stems from the variation of the sample conductance in the numerator, since the change in conductance with signal, g_s, is expected to remain relatively constant. The sample conductance at the operating point decreases by a factor of 67 as the background temperature is decreased from 300° to 4.2°K. The peak responsivity increases by a factor of 57 over this same range.

Although a detailed analysis of the noise mechanism has not yet been made, preliminary measurements indicate that the NEP of this detector at the wavelength of peak responsivity and for f = 260 Hz decreases more than an order of magnitude as the background temperature is reduced from 300° to about 20°K when the detector is operated at 4.2°K. A further decrease in the NEP is expected for operation of the detector at slightly lower temperatures (~3° to 3.5°K).

G. E. Stillman
C. M. Wolfe
J. O. Dimmock

C. GaAs FAR-INFRARED PHOTOCONDUCTIVITY LIFETIME

Lifetime measurements of the extrinsic photoconductivity response of GaAs (Ref. 4) to radiation at 337μ and in one case also at 195μ have been obtained for samples with different donor

-8-9223

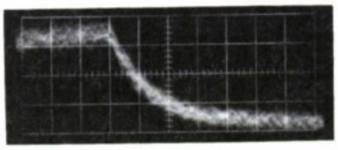

200nsec →| |←

Fig. I-7. Time variation of far-infrared conductivity in GaAs sample 1.

TABLE I-1

FAR-INFRARED PHOTOCONDUCTIVITY LIFETIMES IN GaAs

Sample No.	N_D (cm^{-3})	N_A (cm^{-3})	Wavelength (μ)	Lifetime (nsec)
1	8×10^{13}	4×10^{13}	337	250 ± 30
			195	250 ± 30
2	1.54×10^{14}	2.45×10^{13}	337	250 ± 30
3	1.2×10^{14}	1.0×10^{14}	337	180 ± 30
4	1.1×10^{15}	4.4×10^{14}	337	25 ± 5
5	1.1×10^{15}	3.5×10^{14}	337	23 ± 5

and acceptor concentrations. The measurements were made by passing radiation from a laser through a germanium impact ionization modulator,[5] which acted as a fast chopper, and then onto the GaAs sample, whose conductivity was monitored. Both sample and modulator were at 4.2°K in separate liquid helium dewars. Lifetimes were obtained directly from the decay in sample conductivity, which was observed on an oscilloscope, as shown in Fig. I-7. Results for several samples are given in Table I-1. To a first approximation the lifetime is expected to vary inversely with the number of recombination centers,[6] which at low excitation levels is approximately equal to N_A, the density of compensating acceptors. Although the data do not follow such a simple relationship, the samples with higher N_A have shorter lifetimes, as expected.

T. Holcomb*
I. Melngailis
L. J. Belanger
C. D. Parker

D. IDENTIFICATION OF EXCITON NEUTRAL DONOR COMPLEXES IN THE PHOTOLUMINESCENCE OF HIGH PURITY GaAs

The photoluminescence of high purity ($N_d + N_a \leqslant 5 \times 10^{14}$ cm^{-3}) GaAs epitaxial layers has been studied at low temperatures with a magnetic field. The samples are identical to those used in earlier work.[7,8] For ordinary photoluminescence measurements, the samples were mounted in a strain-free manner in a liquid helium dewar. All spectra shown here were taken at 4.2°K (sample immersed). For the magnetic field measurements the samples were mounted in the axial field of a superconducting solenoid with the excited sample surface normal to the magnetic field ($0 \leqslant \underset{\sim}{H} \leqslant 45$ kG). The samples were excited at near normal incidence using a 100-W Mercury arc or a He-Ne laser. The recombination radiation was gathered from the excited surface of the sample. The sample radiation was dispersed by a Jarrell-Ash 1-meter spectrometer (operated with the resolution shown in the figures) and detected by a cooled S-1 photomultiplier.

The photoluminescence spectrum of a high purity epitaxial layer is shown in Fig. I-8. For this particular sample $N_d = 4.6 \times 10^{13}$ cm^{-3}, $N_a = 3.0 \times 10^{13}$ cm^{-3}, $\mu(77°K) = 195,000$ cm^2/V-sec.

* Summer staff member.

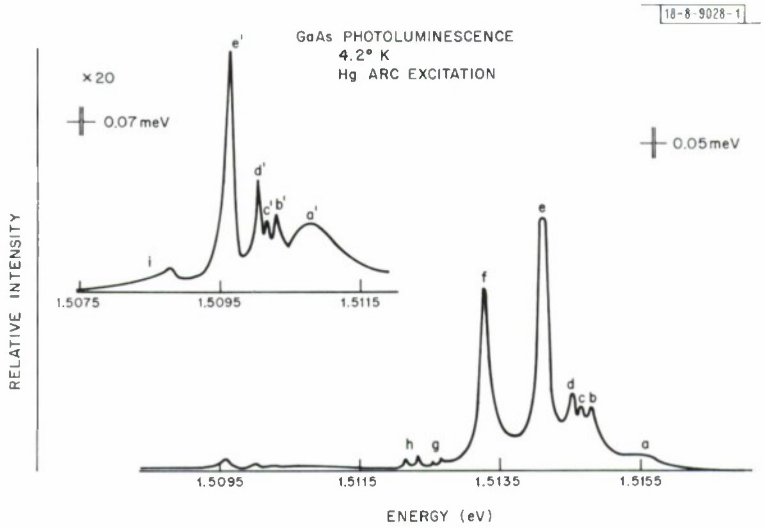

Fig. I-8. Photoluminescence spectrum of high purity GaAs epitaxial layer ($N_D + N_A = 7.6 \times 10^{13}$ cm^{-3}). Inset shows repeated scan (at higher gain) of lower energy portion.

TABLE I-2

ENERGY OF AND SEPARATION BETWEEN SEVERAL PHOTOLUMINESCENCE PEAKS OBSERVED IN FIG. I-8

Peak	Position (eV)	Peak	Position (eV)	Separation (meV)
a	1.5154	a'	1.5109	4.50 ± 0.1
b	1.5148	b'	1.5104	4.42 ± 0.05
c	1.5146	c'	1.5102	4.42 ± 0.05
d	1.5145	d'	1.5101	4.42 ± 0.05
e	1.5141	e'	1.5097	4.42 ± 0.05

The inset in Fig. I-8 shows a scan of the lower energy portion of the spectrum (below 1.5120 eV) at higher gain and signal level. Displayed in this fashion, the low energy series appears to be a close replica of the higher energy set of lines a through e. Because of the relative weakness of line i in the inset we suspect that it is not a replica of the peak f, although the energy spacing is about right. An alternate explanation for this line is given below. We consider here only the two series a-e and a'-e' and are not concerned with recombination at lines f, g and h or at much longer wavelengths (not shown).

The energy of and the separation between each pair of corresponding lines labeled a-a', b-b', etc., is given in Table I-2. The observed energy difference between the lines remains constant near 4.4 meV. This energy difference corresponds to the energy of the $1s \rightarrow 2p$ transition for hydrogenic donors as determined from far-infrared photoconductivity measurements[7] on this same material. This indicates that a neutral donor is involved in all the centers responsible for luminescence peaks a'-e'. We believe the sample luminescence under discussion is proceeding via two mechanisms. The first mechanism gives rise to the high energy series (a through e) and represents some form of direct exciton recombination. The highest energy line "a" has been previously identified as recombination of the free exciton. The lines next to the free exciton but slightly lower in energy (b, c, d and e of Fig. I-8) represent recombination of excitons bound at various centers, all of which we now suspect involve a neutral donor. The second mechanism, giving rise to the low energy series (a' through e' in Fig. I-8 inset), involves a two-electron process in which the exciton recombines leaving the donor in an excited state. The peak a' is probably due to the recombination of a free exciton in the vicinity of the neutral donor, leaving the donor in an excited $n = 2$ state.*

From these arguments we believe that a neutral donor is part of, or in the vicinity of, the centers responsible for peaks b through e and further, that the neutral donor is directly involved in the recombination that establishes peaks a' through e'. The equality of the replica line separations at 4.4 meV indicates that only shallow hydrogenic donors and no deeper donors are involved in the two-electron process. One pair of lines can be associated with exciton recombination at an isolated shallow donor (probably the strongest line e-e'). This leaves the remaining lines b, c, and d to be identified with exciton recombination at various complex centers, all of which involve a neutral shallow hydrogenic donor. From the present data, it is not possible to establish the complete physical nature of the center(s) involved in these recombination processes.

When subjected to a magnetic field, the recombination involving $n = 2$ terminal hydrogenic donor excited states should show the appropriate excited state splittings. All the peaks a', b', c' and d' should show the same magnetic field splittings, but we have been able to measure only that of the dominant line e'. In a magnetic field, the peak e' is observed to split into a quartet e'_1, e'_2, e'_3, and e'_4, corresponding to the different possible $n = 2$ final states of the excited donor center $2p_{+1}$, $2s_0$, $2p_0$, and $2p_{-1}$ respectively. In Fig. I-9 we plot as circles the observed shift and splitting of line e' as a function of magnetic field out to ~40 kG. The triangles mark a combination of experimental results and the solid lines indicate the magnetic field dependence expected from the variational calculation of Larsen.[9]

---

* We suspect that line i is not a replica of peak f but rather is due to a two-electron process involving line e with the donor left in the second excited state. For the hydrogenic donors in this material, the separation between $n = 2$ and $n = 3$ states is 0.8 meV. The peak i appears in energy at 1.5089 eV, exactly 0.8 meV below e', and may be accounted for by recombination involving the second excited state of the donor.

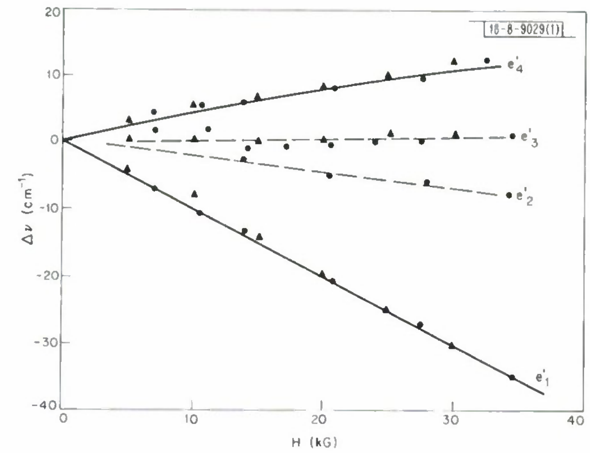

Fig. I-9. Shift and splitting of luminescence peok e' in a mognetic field.

If the luminescence lines e and e' result from exciton recombination at neutral donor with e' corresponding to the donor being left in the n = 2 excited state then, as noted above, the energies of the peaks are related by

$$h\nu(e') = h\nu(e) - E_D(1s \rightarrow 2s, p) \quad ,$$

where $E_D(1s \rightarrow 2s, p)$ is the measured n = 1 to n = 2 shallow donor excitation energy. The triangles in Fig. I-9 are obtained from this expression using the measured position of the line "e" in a magnetic field (to be published) and the far-infrared photoconductivity data from Ref. 7, Fig. 2, for the effect of magnetic field on $E_D(1s \rightarrow 2p_o, p_{\pm 1})$. No far-infrared photoconductivity data exist for $E_D(1s \rightarrow 2s)$ since this transition is not allowed in absorption. The solid lines are drawn using Larsen's theory to calculate both the shift of the exciton ground state in a magnetic field and the effect of a magnetic field on the donor excitation energies $E_D(1s \rightarrow 2p_{\pm 1})$. The energies of the $2p_o$ and 2s states are not calculated in the theory. The fit is obtained assuming an effective mass ratio $\sigma = m_e/m_h \simeq 0.25$ for the exciton bound to the neutral donor. This ratio is, in fact, different from that necessary to fit the shift of the free exciton recombination in a magnetic field $\sigma = 0.375$ and is clearly modified by the effect of the binding center. The excellent agreement between the various data and the solid curves is a strong confirmation that excited 2p states of the neutral donor are observed as terminal states in the two-electron recombination process. This mechanism results in the replication of a high energy set of lines at a lower energy where the energy difference between each pair of corresponding lines is 4.4 meV. The observation of this replica leads us to conclude that a neutral donor (residual, dominant and hydrogenic) is associated with each of these shallow binding centers.

J. A. Rossi
C. M. Wolfe
G. E. Stillman
J. O. Dimmock

E. CONTINUOUS STIMULATED SPIN-FLIP RAMAN SCATTERING IN InSb

Continuous stimulated spin-flip scattering has been observed[10] in InSb, using a CO laser operating in the 5- to 6-μ region. Because of the strong resonance enhancement of the scattering

efficiency which occurs due to pumping near the direct bandgap of InSb, thresholds as low as 200 mW in an estimated 100-μ beam diameter within the crystal have been observed. Patel and Shaw[11] have reported the first observation of stimulated spin-flip scattering in InSb, using a Q-switched CO_2 laser operating at 10.6μ and found thresholds as low as 200 W in the crystal.

The CW stimulated spin-flip scattering experiments were performed by using a liquid-nitrogen-cooled CO laser[12] whose output wavelength could be chosen from any of about sixty lines between 5.2 and 6.0μ by using a grating as one of the cavity mirrors. The nominal multimode output in some of the strongest lines is limited only by the size and efficiency of the laser, with several watts in a single line being easily achieved in a one-meter tube. Room temperature operation of the CO laser has also been achieved with comparable output powers.[13]

Figure I-10 shows the spectrum of the scattered light collected along the magnetic field, $\vec{H}$ (35 kG) for the incident light across $\vec{H}$, below (lower trace) and above (upper trace) the threshold for stimulated scattering. The lower trace shows the spontaneous spin-flip scattering peak shifted in frequency by $\Delta\omega = 72\ \mathrm{cm}^{-1}$ from the incident CO laser line at 5.32μ. The frequency shift is given by $\Delta\omega = g\beta H$, where g is the conduction electron g-factor and β is the Bohr magneton. The upper trace shows two stimulated Stokes lines occurring for a factor of two increase in pump intensity. There is enough intensity in the first Stokes line to produce this second stimulated spin-flip line, thus increasing the tuning range of this oscillator.

A plot of the relative spin-flip power as a function of input laser power in the sample is shown in Fig. I-11. The scattered light was collected along $\underset{\sim}{H}$ and the input laser was chopped with a 6-percent duty cycle. The 200-mW threshold was obtained with only the natural 36-percent reflecting surfaces of InSb. This is the lowest threshold power ever obtained for a Raman oscillator.

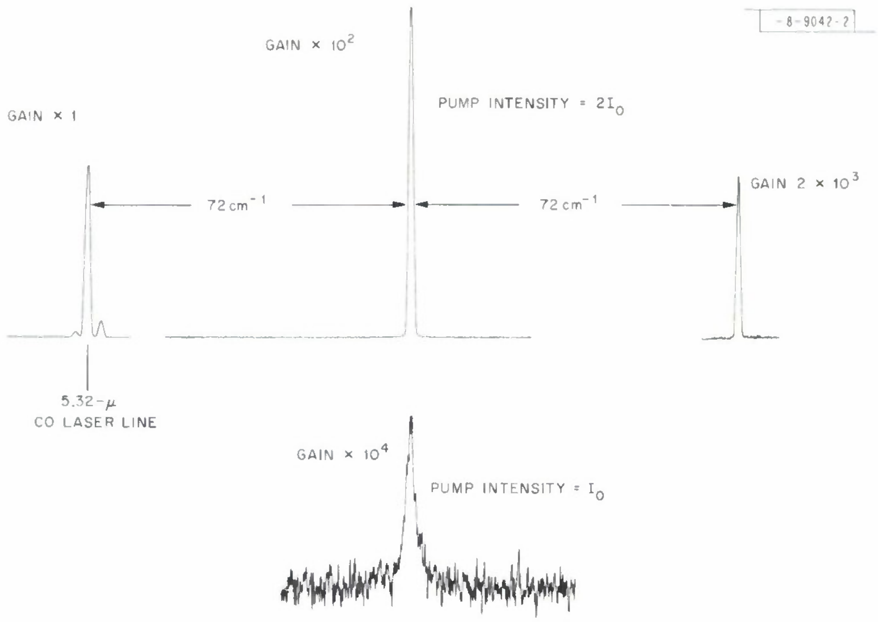

Fig. I-10. Scattered light intensity versus wavelength showing the spontaneous (lower trace) spin-flip line and two stimulated peaks (upper trace) at positions corresponding to one and two spin-flip energies from the pump line at 5.32 μm. (H = 35 kG, concentration ~$1 \times 10^{16}\ \mathrm{cm}^{-3}$, T ~ 30°K.)

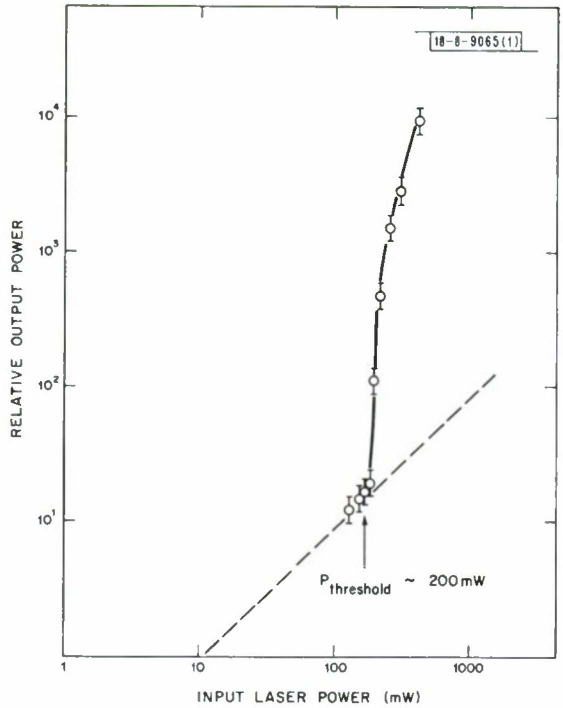

Fig. I-11. Spin-flip Ramon output power versus pump power in InSb ($n = 1 \times 10^{16}$ cm^{-3}, H = 35 kG, λ_{pump} = 5.32 µm, T ~ 30°K).

Resonance enhancement of the spontaneous spin-flip Raman scattering efficiency, S, provides the largest single contribution to the low thresholds which have been observed. The spin-flip Raman scattering efficiency for no change of orbital momentum near resonance is given by[14]

$$S = 2.1 \times 10^{-23}\, n\left(\frac{\omega_2}{\omega_1}\right)\left[\frac{\omega_g \omega_1}{\omega_g^2 - \omega_1^2}\right]^2 ,$$

where $\omega_g \simeq 1/\hbar\,(\epsilon_g + \frac{1}{2}\hbar\omega_c - \frac{1}{2}g\beta H)$ is the optical bandgap frequency in a magnetic field, ω_c is the cyclotron frequency and n is the electron concentration. The calculated scattering efficiency for InSb at 35 kG, 0°K, and $n = 1 \times 10^{16}$ cm^{-3}, using a 5.32-µ laser, is $S = 1.5 \times 10^{-4}$ cm^{-1} sr^{-1}.

The Raman gain for a Stokes wave is calculated from the expression[15]

$$G = \frac{8\pi^2 c^2}{\hbar\omega_2^3}\,\frac{SI}{n_S^2(n_o + 1)\,\Delta\omega} ,$$

where n_2 is the refractive index at the Stokes frequency, n_o is the Boson occupation factor, $\Delta\omega$ is the half-width of the Raman line, and I is the pump intensity in W/cm^2. The calculated gain for the above conditions is $G = 9 \times 10^{-4}$ I cm^{-1}, which gives a threshold comparable to that observed.

CW stimulated Raman scattering can greatly facilitate the study of the stimulated Raman effect, as well as provide a useful tunable source in the infrared. The use of $Hg_xCd_{1-x}Te$ or $Pb_xSn_{1-x}Te$ alloy crystals whose bandgaps are resonant at the CO, CO_2 or any other laser wavelength may provide a greater range of tunability as well as CW operation. Useful CW power

outputs of several watts in a diffraction-limited mode appear possible with a broad tuning range in the near-to-middle infrared region.

A. Mooradian
S. R. J. Brueck
F. A. Blum

F. HIGH-SPEED $Hg_{1-x}Cd_xTe$ PHOTODIODES

$Hg_{1-x}Cd_xTe$ photodiodes with a fast response at 77°K have been fabricated by Hg-diffusion from crystals grown by a new method.[16] External quantum efficiencies of 20 percent were measured and frequency response to beyond 1 GHz was observed at 10.6-μ wavelength by heterodyning a tunable $Pb_{0.88}Sn_{0.12}Te$ diode laser with a fixed-frequency CO_2 laser.

The crystals which had a Cd content (x) of 0.18 were p-type with a carrier concentration of 2×10^{17} cm^{-3}. After etching in a 5-percent bromine-methanol solution, an n-type layer about 5μ deep was formed by diffusing in Hg at 320°C for 10 minutes. A number of mesa-type elements (0.06 to 0.12 mm^2 area) were then separated on one face of the slice by masking and etching. Contact to the elements was made by evaporating 100-μ-diameter indium circles to which leads were subsequently indium-bonded. Contact to the common p-side was made by plating first a layer of gold and then a layer of indium. The junction depth was further reduced by etching the n-type surface following diffusion in order to improve the quantum efficiency.

Measurements were made with the detector package mounted to a cold-finger in a liquid nitrogen dewar. The spectral response peaked at 14μ and had a cutoff at 17μ. External quantum efficiency, limited by reflection and recombination losses, was 13 percent with no bias applied to the diode. The zero-bias dynamic impedance was 15 ohms for a 0- to 12-mm^2 area device, and the peak detectivity was 3×10^9 cm$\sqrt{\text{Hz}}$/W. With a reverse bias of 0.3 V, the quantum efficiency increased to 20 percent as expected due to improved carrier collection in the wider depletion region, and the dynamic impedance was 30 ohms.

The frequency response measurements were made in a manner described earlier for $Pb_{0.80}Sn_{0.20}Te$ photovoltaic detectors[17] and for Ge:Cu photoconductors.[18] Figure I-12 shows the frequency response of a $Hg_{0.82}Cd_{0.18}Te$ photovoltaic detector at a reverse bias of 0.5 V.

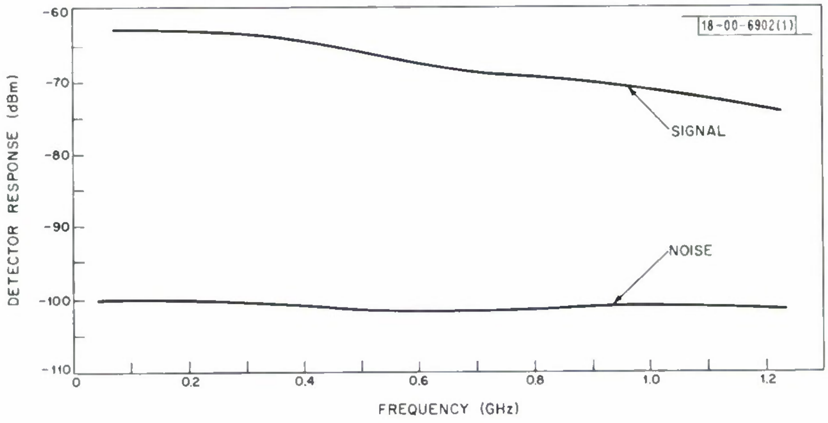

Fig. I-12. Frequency response of $Hg_{0.82}Cd_{0.18}Te$ photodiode at 77°K. Applied reverse bias is 0.5 V. Noise level is due to a wideband preamplifier with 5.1-dB maximum noise figure over frequency range shown.

The 3-dB point occurs at about 500 MHz; however, a substantial signal is observed out to 1.2 GHz where the response has dropped by about 10 dB. The dynamic impedance of the detector at 0.5 V reverse bias was about 20 ohms, thus providing an acceptable match to the 50-ohm line and the 50-ohm input impedance of the preamplifier. Local-oscillator noise-limited operation was observed at 250 MHz with about 60-mW CO_2 laser power and a preamplifier having a 4-dB noise figure.

I. Melngailis
T. C. Harman
E. D. Hinkley

REFERENCES

1. Solid State Research Report, Lincoln Laboratory, M.I.T. (1970:3), p. 2.
2. Op. cit. (1970:2), p. 1.
3. R. F. Wallis and H. Shenker, NRL Report 5996 (1963), p. 14.
4. G. E. Stillman, C. M. Wolfe, I. Melngailis, C. D. Parker, P. E. Tannenwald and J. O. Dimmock, Appl. Phys. Letters 13, 83 (1968).
5. I. Melngailis and P. E. Tannenwald, Proc. IEEE (Letters) 57, 806 (1969).
6. M. Lax, Proceedings of the Photoconductivity Conference, Atlantic City, N.J., 1954 (Wiley, New York, 1956), p. 135.
7. G. E. Stillman, C. M. Wolfe and J. O. Dimmock, Solid State Commun. 7, 921 (1969).
8. C. M. Wolfe, G. E. Stillman and J. O. Dimmock, J. Appl. Phys. 41, 504 (1970).
9. D. M. Larsen, J. Phys. Chem. Solids 29, 271 (1968).
10. A. Mooradian, S. R. J. Brueck and F. A. Blum, Appl. Phys. Letters (to be published).
11. C. K. N. Patel and E. D. Shaw, Phys. Rev. Letters 24, 451 (1970).
12. R. M. Osgood, W. E. Eppers and E. R. Nichols, IEEE J. Quant. Electron 6, 145 (1970).
13. M. L. Bhaumik, Appl. Phys. Letters 17, 188 (1970).
14. Y. Yafet, Phys. Rev. 152, 858 (1966); G. B. Wright, P. L. Kelley and S. H. Groves, in Light Scattering Spectra of Solids, G. B. Wright, Ed. (Springer-Verlag, New York, 1969), p. 335.
15. W. D. Johnson, Jr. and I. P. Kaminov, Phys. Rev. 168, 1045 (1968).
16. Solid State Research Report, Lincoln Laboratory, M.I.T. (1970:3), p. 2.
17. Optics Research Report, Lincoln Laboratory, M.I.T. (1970:2), p. 1.
18. Solid State Research Report, Lincoln Laboratory, M.I.T. (1968:3), p. 19, DDC AD-678534.

II. MATERIALS RESEARCH

A. PARTIAL AND TOTAL VAPOR PRESSURES OVER MOLTEN Bi_2Te_3

In order to resolve discrepancies among the published data for the total and partial vapor pressures over solid Bi_2Te_3 (Refs. 1, 2, 3), the total pressure over liquid Bi_2Te_3 (Ref. 4), and the partial pressure of Te_2 over solid and liquid Bi_2Te_3 (Ref. 5), we have used a new manometric technique to determine the total pressure over $Bi_2Te_3(\ell)$ and have also extended our earlier optical density measurements[5] to higher temperatures.

To explain the principle of the manometric technique, we refer to the schematic of the high temperature part of the apparatus shown in Fig. II-1(a). The manometer cell, shown in detail in Fig. II-1(b), consists essentially of an inverted fused silica U-tube whose open ends are immersed in a reservoir of molten Bi_2Te_3 contained in a silica crucible. Argon pressure from an external source is applied to the surface of this reservoir through a long silica capillary, shown

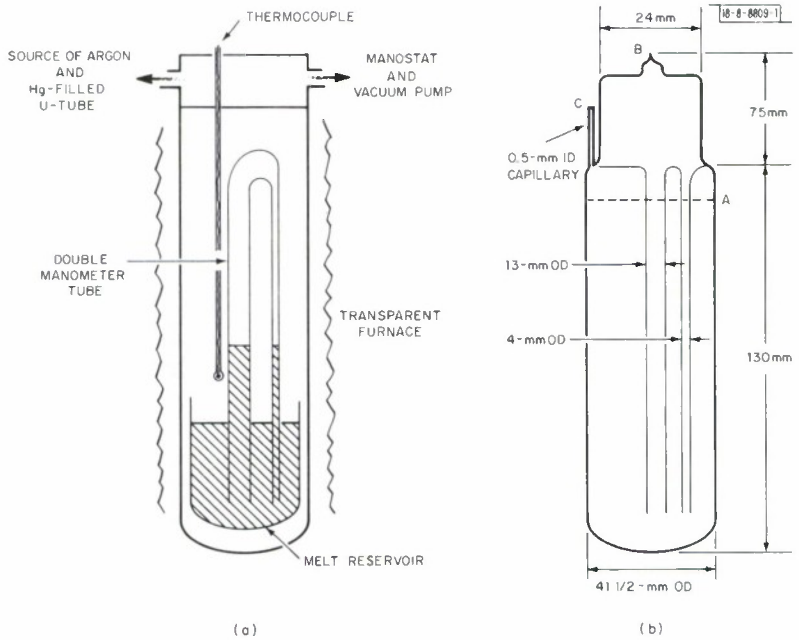

Fig. II-1. Apparatus for measuring total vapor pressure over a melt by manometric technique.

schematically at C in Fig. II-1(b). When this pressure is varied, the height of the melt in each leg of the U-tube changes until the pressure inside that leg at the level of the reservoir surface equals the pressure on the reservoir surface outside the U-tube. Provided that no residual foreign gas is trapped in the U-tube, the inside pressure is the sum of the total vapor pressure over $Bi_2Te_3(P'_\Sigma)$, the hydrostatic pressure of the column of molten Bi_2Te_3 of height h above the reservoir surface, and a term due to capillary action. The outside pressure is equal to the argon

pressure measured external to the cell, P_{ex}. If the outside and inside pressures are set equal

$$P_{ex} = P'_{\Sigma} + hd_M g + \frac{2\gamma_M}{r} \quad , \tag{1}$$

where P_{ex} and P'_{Σ} are expressed in dynes/cm^2, and h is in centimeters. The quantities d_M (in g/cm^3) and γ_M (in dynes/cm) are, respectively, the density and surface tension of molten Bi_2Te_3, g is the acceleration due to gravity, and r is the radius of the U-tube leg in centimeters.

If the external measurement of argon pressure is made by means of a mercury-filled U-tube, $P_{ex} = Hd_{Hg}g$, where H is the difference in centimeters between the mercury levels in the two arms and d_{Hg} is the density of mercury. Then Eq. (1) can be rewritten as

$$H = P_{\Sigma} + h(d_M/d_{Hg}) + \frac{2\gamma_M}{rd_{Hg}g} \quad , \tag{2}$$

where $P_{\Sigma} \equiv P'_{\Sigma}/d_{Hg}g$ is the total vapor pressure of the melt expressed in centimeters of mercury. In our experiments, the values of h were the same within experimental error for the two legs of the U-tube, whose radii differed by a factor of four. This showed that the capillary force term could be neglected. Omitting this term from Eq. (2) and rewriting gives

$$h = (d_{Hg}/d_M)\, H - (d_{Hg}/d_M)\, P_{\Sigma} \quad . \tag{3}$$

Therefore, a plot of h as a function of H should give a straight line which yields the values of P_{Σ} (equal to H when h = 0) and d_M (equal to the reciprocal slope times d_{Hg}). If residual gas is trapped in the upper part of the U-tube, the pressure it exerts will cause deviations from linearity at sufficiently high values of H, with the slope decreasing as H increases.

In order to make the pressure measurements, the manometer cell shown in Fig. II-1(b) was first loaded with about 360 grams of Bi_2Te_3 prepared by fusing the elements in stoichiometric proportions. It was then placed in the apparatus shown schematically in Fig. II-1(a). The cell rested on the bottom of a long silica tube closed at the top with a brass cap that provided a central entry for a thermocouple tube and had two side ports, one connecting to a mechanical vacuum pump through a mercury manostat and the other connecting to an argon cylinder. A side arm on the line to the argon cylinder led to a vertical mercury-filled U-tube, one arm of which was evacuated, and to a Dubrovin gauge. The manometer cell was centered in a resistance furnace consisting of three adjacent zones, each heated by eight equispaced, concentrically placed vertical wires enclosed in insulators. This open-structured furnace was in turn surrounded by a Pyrex tube, the interior of which was covered by a vacuum-deposited gold film about 30 to 50 nm thick. The gold layer was sufficiently transparent in the visible to permit observation of the melt levels in the cell, while simultaneously reflecting and containing most of the infrared radiation from the furnace.

With the manometer cell in place, the long silica tube was evacuated and the cell was heated to 640°C for about 2 hours to melt the Bi_2Te_3 and seal the manometer legs. An argon pressure of 10 cm Hg was then admitted to start the measurements. For each determination of the vapor pressure the power to the three furnace zones was adjusted until the temperatures at points A and B in Fig. II-1(b) and at the bottom of the manometer cell were within 3°C of each other.

After the external argon pressure had been set, the levels of the melt in the two legs of the manometer and in the silica crucible, and the levels in the two arms of the mercury U-tube, were read to the nearest 0.005 cm with a cathetometer to determine h and H. For pressures below 2 cmHg, H was also read with the Dubrovin gauge. After a change in the argon pressure, usually 30 to 40 minutes were required until the levels of the Bi_2Te_3 melt in the manometer cell became constant. The disadvantage of this long time constant, caused by the restricted access through the long capillary into the cell, was accepted in order to minimize the loss of material from the cell by vaporization.

Pressure measurements were made at eight temperatures between 707° and 896°C. At each temperature, readings were taken for 3 to 7 values of the argon pressure. When the apparatus was left overnight, the temperature was lowered to 600°C (about 15°C above the melting point of Bi_2Te_3) and H held at 12 to 15 cmHg. A total of nine days was taken to complete the measurements, after which the apparatus was cooled to room temperature and the Bi_2Te_3 removed and weighed. The weight loss was 3.2 g, putting an upper limit of ±0.5 at.% Te on the change in composition resulting from vaporization.

TABLE II-1

TOTAL VAPOR PRESSURE AND DENSITY OF $Bi_2Te_3(\ell)$

$10^3/T$	Data Points	Range in h (cm)	$\sigma(h)$ (cm)	$d \pm \sigma(d)$ (g/cm^3)	$P_\Sigma \pm \sigma(P_\Sigma)$ (atm)
1.021	6	0.27 – 11.64	0.050	7.288 ± 0.068	$(5.84 \pm 0.34)\,10^{-3}$
0.9970	5	0.365 – 8.34	0.035	7.240 ± 0.081	$(8.39 \pm 0.31)\,10^{-3}$
0.9588	4	0.62 – 10.64	0.008	7.473 ± 0.013	$(1.34 \pm 0.009)\,10^{-2}$
0.9268	6	0.54 – 9.46	0.030	7.438 ± 0.054	$(2.19 \pm 0.02)\,10^{-2}$
0.9025	6	0.13 – 7.86	0.024	7.079 ± 0.054	$(3.06 \pm 0.01)\,10^{-2}$
0.8554	3	2.31 – 5.85	0.004	6.994 ± 0.027	$(5.93 \pm 0.00)\,10^{-2}$
0.9615	4	1.68 – 7.64	0.011	7.265 ± 0.027	$(1.25 \pm 0.02)\,10^{-2}$
1.000	7	0.95 – 9.5	0.030	7.406 ± 0.054	$(8.28 \pm 0.03)\,10^{-3}$

h is the height of $Bi_2Te_3(\ell)$ in the manometer tube, d is the density, and P_Σ is the total vapor pressure. $\sigma(i)$ is the standard deviation in i.

The results of the manometer measurements on $Bi_2Te_3(\ell)$ are summarized in Table II-1, which lists the runs in chronological order. For each run, the table gives the values of the density (d) and total pressure (P_Σ) found according to Eq. (3) from the slope and intercept of the straight line obtained by a least-squares fit to the data for h as a function of H. The densities are plotted against temperature in Fig. II-2, which also shows the density values measured

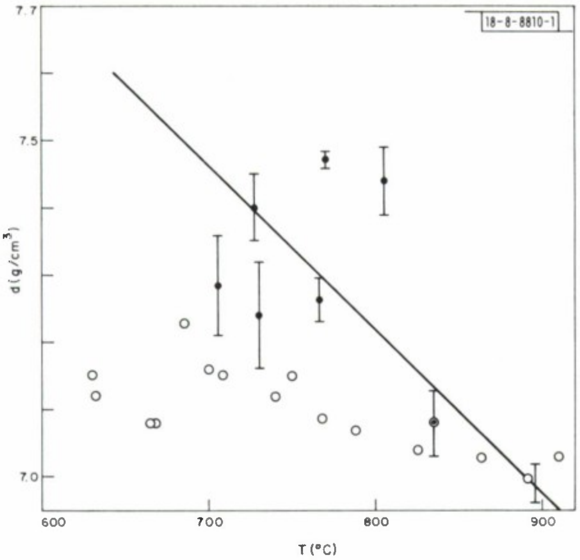

Fig. II-2. Density (d) of $Bi_2Te_3(\ell)$ as o function of temperature. Present dato are shown with error bors ot ± one stondord deviation. Open circles ore from Ref.6.

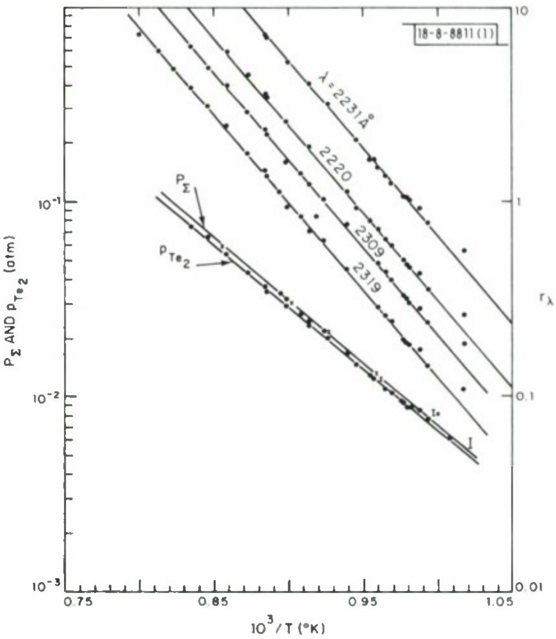

Fig. II-3. Two lowest lines: temperature dependence of total vapor pressure (P_Σ) ond portiol pressure of Te_2 (p_{Te_2}) over $Bi_2Te_3(\ell)$.

Four upper lines: temperature dependence of portiol optical densities (r_λ), ot indicated wavelengths, due to BiTe(g) over $Bi_2Te_3(\ell)$.

elsewhere by a pycnometric technique.[6] The agreement is reasonably good. The densities for four of our runs appear to be high, but these possible errors in density apparently are not associated with any scatter in the corresponding values of P_Σ.

The values of P_Σ obtained by the manometer measurements are plotted on a logarithmic scale against reciprocal absolute temperature in Fig. II-3. The line representing these values is given by

$$\log_{10} P_\Sigma(\mathrm{atm}) = -6.4691(10^3)/T + 4.3219 \qquad 1.02 \geqslant 10^3/T \geqslant 0.85 \quad . \qquad (4)$$

This line is almost parallel to the one obtained by Ustygov,[4] who determined P_Σ by means of Bourdon gauge measurements, but our values are about 35 percent less than his.

In addition to measuring the total pressure of the vapor over $Bi_2Te_3(\ell)$, we have investigated the composition of the vapor by means of optical absorption measurements. The optical density ($D = \log I_0/I$) of the vapor in a fused silica optical cell at a fixed temperature (1000°C) was measured over the wavelength range between 1990 and 7000 Å as a function of the temperature (670° to 930°C) of a sidearm reservoir containing $Bi_2Te_3(\ell)$. The details of the experimental technique have been described in Ref. 5. The absorption spectrum of the vapor appears to be a superposition of the spectrum for $Te_2(g)$ and that of another species which shows vibronic bands between 2000 and 2450 Å, where the $Te_2(g)$ spectrum has no structure. Runs using a pure Bi reservoir showed that the additional bands are not due to $Bi_2(g)$ or Bi(g). We conclude that these bands are due to BiTe(g), which has been detected in mass spectrographic studies[7] as a major species over $Bi_2Te_3(\ell)$. Our experiments indicate that the sum of the partial pressures of $Te_2(p_{Te_2})$ and BiTe(p_{BiTe}) is within 3 percent of the total vapor pressure of $Bi_2Te_3(\ell)$. Therefore, to a good approximation, we can write

$$P_\Sigma = p_{Te_2} + P_{BiTe} \quad . \qquad (5)$$

Values of p_{Te_2} were determined from the optical densities measured at 4357, 5000, and 5500 Å, where BiTe(g) does not absorb appreciably, by using calibration curves obtained from optical density measurements made with a pure Te reservoir. The p_{Te_2} values are plotted on a logarithmic scale against reciprocal absolute temperature along the lowest straight line in Fig. II-3. The equation for this line is

$$\log_{10} p_{Te_2}(\mathrm{atm}) = -6.3048(10^3)/T + 4.1396 \qquad 1.02 \geqslant 10^3/T \geqslant 0.85 \quad . \qquad (6)$$

Partial optical densities (r_λ) of BiTe(g) at four of its absorption maxima (λ = 2200, 2231, 2409 and 2319 Å) were calculated by subtracting the partial optical density of $Te_2(g)$ from the total optical density observed at each wavelength. The $Te_2(g)$ contributions were determined from the total optical densities measured at 4357, 5000 and 5500 Å, where the absorption is due entirely to $Te_2(g)$, by using data for optical density as a function of wavelength measured in calibration experiments with a pure $Te(\ell)$ reservoir. The values of r_λ for BiTe(g) obtained in this way are plotted against the reciprocal absolute temperature of the $Bi_2Te_3(\ell)$ reservoir in Fig. II-3. The data are well represented by four parallel straight lines, consistent with the assumption that they represent absorption by a single vapor species that satisfies Beer's law.

In order to determine p_{BiTe} from the optical absorption data, it is neeessary to know the values of the Beer's law constant α_λ which relate p_{BiTe} and r_λ

$$p_{BiTe} = \alpha_\lambda r_\lambda \quad . \tag{7}$$

Calibration data giving these values cannot be obtained in the same direct manner as those for $Te_2(g)$, since a vapor phase consisting entirely of BiTe(g) does not exist. However it was possible to determine α_λ from the present data by comparing the results of the manometric and optical absorption measurements. According to Eq. (5), p_{BiTe} can be calculated as a function of temperature by subtracting the values of p_{Te_2} given by Eq. (6) from the values of P_Σ given by Eq. (4). The constants adopted for Eq. (6) were adjusted to give a temperature dependenee of p_{BiTe} most nearly the same as that observed for the r_λ values plotted in Fig. II-3. This procedure yields an average value of $\alpha_{2231} = 4.35 \times 10^{-4}\,\mathrm{atm}^{-1}$ for an optical path length of 99.9 mm at 1000°C. The resulting equation for p_{BiTe} is

$$\log_{10} p_{BiTe}(\mathrm{atm}) = -8.978(10^3)/T + 5.4432 \quad . \tag{8}$$

According to Eqs. (4), (6) and (8), the Te content of the vapor over $Bi_2Te_3(\ell)$ varies from 98 at. % Te at 700°C to 95 at. % Te at 900°C. Thus the Te content greatly exceeds 60 at. %, and $Bi_2Te_3(\ell)$ vaporizes incongruently over the entire temperature range investigated. Preliminary analysis of our earlier optical absorption results[5] indicates that solid Bi_2Te_3 also vaporizes incongruently, although several other groups[1,2,3] have eoneluded that it vaporizes congruently.

R. F. Brebrick
F. T. J. Smith

B. HIGH-PRESSURE $RbFeCl_3$ – A TRANSPARENT FERRIMAGNET

At atmospheric pressure, the structure [Fig. II-4(a)] of $RbFeCl_3$ (Ref. 8) contains hexagonal close-packed $RbCl_3$ layers with Fe filling all the chlorine octahedra. We prepared the compound by heating an equimolar mixture of RbCl and $FeCl_2 \cdot 4H_2O$ in flowing dry HCl or dry nitrogen at 500°C. Since $RbFeCl_3$ is hygroscopic, all handling of the atmospheric and high-pressure forms was done in a glove bag filled with dry nitrogen. X-ray diffraction patterns were obtained using monochromated (LiF crystal) CuK_α radiation with a diffractometer entirely enclosed in a large glove bag filled with dry nitrogen. To prepare high-pressure phases, samples of freshly prepared $RbFeCl_3$ contained in gold eapsules (4-mm diameter × 10 mm) were first subjeeted to the desired pressure (up to 80 kbars) in a belt apparatus and then brought rapidly to 650°C with an internal graphite heater. After a half-hour to an hour at temperature, the samples were rapidly quenched before the pressure was released.

Three high-pressure phases (designated at 9R, 6H and 3C) were obtained, with the proportion of cubic close packing increasing with increasing pressure, as previously observed in similar experiments on ABF_3 compounds.[9,10] The characteristics of these phases are summarized in Table II-2 and their structures are shown in Fig. II-4. The stability at atmospheric pressure of the three quenched high-pressure phases deereased as the amount of eubie elose packing increased. For starting material prepared in dry HCl, at room temperature the 9R form showed

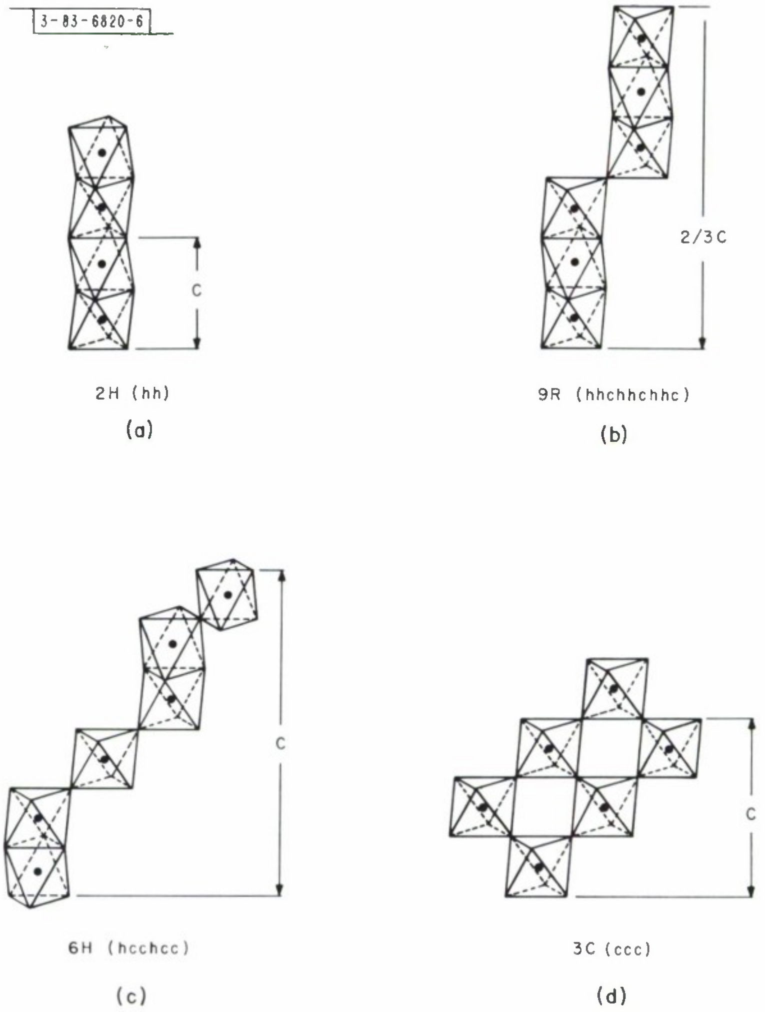

Fig. II-4. Octahedra linkages of four polytypes found for $RbFeCl_3$.

TABLE II-2

HIGH PRESSURE POLYTYPES OF $RbFeCl_3$

Structure	Pressure Range (kbars)	Cell Dimensions (Å) ± 0.1%	Vol/$RbFeCl_3$(Å^3)
2H	<15	$\underline{a}$ = 7.060 $\underline{c}$ = 6.020*	129.9
9R	15 – 20	$\underline{a}$ = 7.05 $\underline{c}$ = 26.2	125.3
6H	20 – 35	$\underline{a}$ = 7.04 $\underline{c}$ = 17.35	124.0
3C	>35	$\underline{a}$ = 4.975	123.1

*Ref. 8.

no evidence of retransformation to the 2H form, the 6H form retransformed over a period of a week and the highest-pressure, perovskite 3C form retransformed in about a day. The stability of all high-pressure phases was dependent on the preparation conditions of the atmospheric pressure form. If the starting material was prepared in dry nitrogen, the stability of the high-pressure phases increased dramatically; they required heating at 400°C for a few hours to effect a retransformation and were not as hygroscopic as those prepared in an HCl atmosphere.

Magnetic susceptibility measurements have been made on powdered samples of the 6H and perovskite high-pressure forms of $RbFeCl_3$ with a vibrating-sample magnetometer calibrated with Ni. Samples of 40 to 150 mg were studied from 4.2°K to room temperature and in fields up to 17 kOe. The magnetic properties of the 9R form were not studied because it could not be obtained as a single phase. Because of its very narrow (~5 kbars) stability region, the small pressure gradients present during our preparations always produced some 2H or 6H form along with the 9R form.

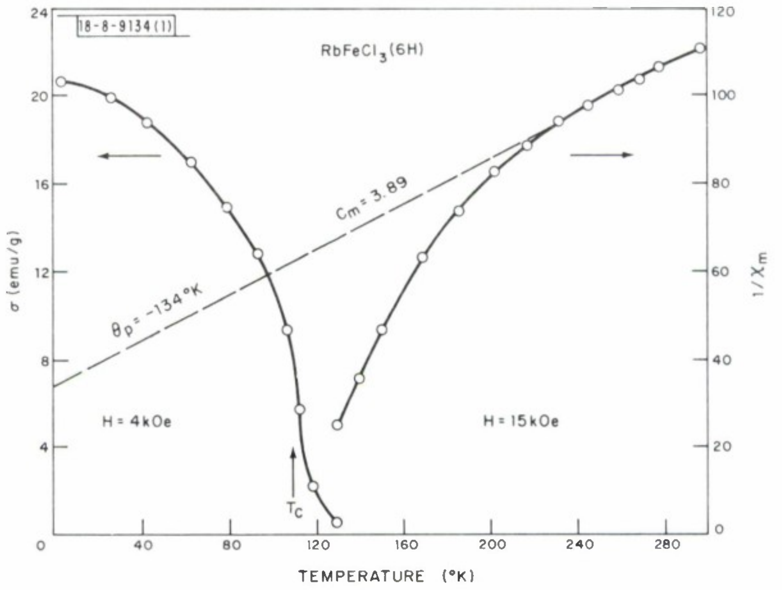

Fig. II-5. Magnetization as a function of temperature for powdered 6H form of $RbFeCl_3$.

The 6H form of $RbFeCl_3$ is ferrimagnetic with T_c = 109°K, determined from the inflection point in the susceptibility obtained at very low fields. Above T = 230°K (see Fig. II-5) the susceptibility obeys the Curie-Weiss law with C_M = 3.89 emu-°K/mole ($\mu_{eff} \equiv \sqrt{(8C_M)}$ = 5.58 μ_B) and θ_p = −134°K. The high μ_{eff} found (in comparison, μ_{eff} = 4.90 μ_B for spin-only high-spin Fe^{2+}) is attributed to strong orbital contributions to the magnetic moment. The isostructural $CsFeF_3$ has μ_{eff} = 5.65 μ_B (Ref. 11) while the structurally related perovskite $RbFeF_3$ has 5.8 μ_B (Ref. 12) and the atmospheric pressure form of $RbFeCl_3$ has 5.8 to 6.1 μ_B (Ref. 13).

The saturation magnetization (σ_o) determined for 6H-$RbFeCl_3$ from a 1/H versus M plot in fields up to 17.2 kOe is 1.1 μ_B (25.4 emu/g) while for isostructural $CsFeF_3$ σ_o measured on powders is 1.2 to 1.3 μ_B (Refs. 11-14). The magnetic ordering of the Fe^{2+} ions is probably similar to the ordering in the 6H form of $CsFeF_3$ or to the ordering of Ni^{2+} ions in the 6H forms of

$RbNiF_3$ and $CsNiF_3$. Pairs of face-shared octahedra (90° Fe-Cl-Fe) are ferromagnetically ordered while the corner-shared octahedra (180° Fe-Cl-Fe) are antiferromagnetically ordered [Fig. II-4(c)], so that the spins of four Fe are aligned in one direction and two in the opposite direction. Our low saturation magnetization ($1.1\,\mu_B$ versus $1.33\,\mu_B$ theoretical) may be attributed to a high magnetocrystalline anisotropy for this hexagonal strueture. However, one cannot rule out a more complex, noncollinear spin structure such as that found for $CsFeF_3$ (Ref. 15).

The change in T_c with hydrostatic pressure, as determined in a vibrating-coil magnetometer using He gas as the pressure transmitting agent,[16] was linear to 8 kbars with $dT_c/dP = +2.13 \pm 0.05$ deg/kbar. This value is about four times larger than those found for the isostructural fluorides $RbNiF_3$ (Ref. 17) (+0.60 deg/kbar) and $CsNiF_3$ (Ref. 18) (+0.53 deg/kbar) and reflects the higher covalency and significantly higher compressibility of the ehloride ion.

Optical transmission data were collected on a 1:100 $RbFeCl_3$:KBr mixture which was finely ground and pressed into a disk at 6 kbars and 60°C. The tan ferrimagnetic material was studied from 0.3 to 24 μm and showed transparency over this entire range, except for some absorption bands from 0.3 to 0.7 μm that are similar to those reported for isostructural $CsFeF_3$ (Ref. 15).

The details of the magnetic properties of the perovskite form of $RbFeCl_3$ could not be determined due to the presence of a second phase. If the starting material was prepared in dry nitrogen, the perovskite was always contaminated with very small amounts of Fe_3O_4. If the starting material was prepared in dry HCl, the perovskite began to retransform quickly to the atmospheric-pressure 2H form. Magnetic data were collected on samples that contained about 10 percent of the 2H form. No ferri or ferromagnetic transitions were observed to 4.2°K. However, there was a small spontaneous moment at 4.2°K that gradually decreased with increasing temperature, disappearing at about 100°K. This behavior would be consistent with ferromagnetic coupling within the face-shared chains of the 2H form, as suggested by the susceptibility of the pure phase.[13]

J. M. Longo   K. Dwight
J. A. Kafalas   D. A. Batson
N. Menyuk   D. M. Tracy

C. HIGH-PRESSURE SYNTHESIS

A review of high-pressure synthesis, as illustrated by studies on compounds with the chemical formula ABX_3 or $(AX)_n(ABX_3)$, has been prepared for publication as a chapter entitled "High-Pressure Syntheses" in Preparative Methods in Solid State Chemistry, edited by P. Hagenmuller (Academic Press, New York). The Introduction is given below.

> "High-pressure synthesis has a practical as well as a scientific interest, since many high-pressure products are either stable or metastable at atmospheric pressure to temperatures well above 300°K. To illustrate the strategy and present-day techniques of high-pressure synthesis, we have chosen to review the high-pressure studies – through June 1970 – performed on compounds having the chemical formula ABX_3 or $(AX)_n(ABX_3)$, where cation A is always larger than cation B. At atmospheric pressure, these compounds crystallize in a variety of different structures, or do not form at all. High pressures stabilize preferentially the more dense phase. The most dense ABX_3 phase has the cubic-perovskite structure, and if the

A eation is not too small, pressures obtainable in the laboratory are generally sufficient to stabilize it. In the case of oxides, fluorides and ehlorides, these high-pressure perovskites, as well as the intermediate-pressure polymorphs, are generally stable at atmospherie pressure and room temperature.

After a brief deseription in See. II of general preparative techniques, several ABX_3 and $(AX)_n(ABX_3)$ struetures are eompared in See. III, special attention being given to eation-site coordinations and relative densities. The experimental summary is divided into three operational groupings:

(1) High-pressure transformations of eompositions prepared at atmospherie pressure

(2) Composition formations requiring elevated pressures

(3) Syntheses greatly faeilitated by pressure

Within thc first grouping, the relative stabilities of five hexagonal-perovskite polytypes are determined by the relative ionic sizes and the pressure. Thcse polytypes are distinguished from the other polymorphs, sinee extensive data on the relationships between them are now available. The relative stabilities of other ABX_3 polymorphs depend upon the outer-eleetron eonfigurations at the eations as well as on relative ionie sizes and pressure. Some general features of these inter-rclationships arc presented. They permit elassifieation of the seeond grouping into six distinguishable groupings, eaeh representing a different set of eonditions, modifiable by high pressure, that inhibit eomposition formation at atmospheric pressure. In all cases, high pressure stabilizes prcferentially a more dense phase. This classifieation is not intended to be exhaustive, but to illustrate, from available data on ABX_3 eompounds, eonsidcrations pertinent to the choice of high pressure as a tool for chemical synthcsis. The final scetion merely ealls attention to the faet that high pressure may also alter the kineties of a reaetion so as to greatly faeilitate synthcsis of a eomposition stable at atmospherie pressure."

J. B. Goodenough
J. M. Longo
J. A. Kafalas

D. VOLUME COMPRESSION OF TiO_x

Preliminary data were reeently reported[19] for the volume eompression of cubic titanium monoxide, determined with diamond-anvil high-pressure x-ray diffraetion units. Additional data have been obtained by the same teehniques, using primarily the two serew-loaded units deseribed.[19] The decrease in lattiee parameter and cell volume as a funetion of pressure up to 100 kbars ean now be reliably reported for the compositions $TiO_{0.85}$, $TiO_{1.0}$, $TiO_{1.11}$ and $TiO_{1.25}$. The experimental problems[20] involved with these measurements, partieularly on materials sueh as these with very low volume eompressibilities, eause appreeiable seatter in the data points for an individual pressure run. However, when a set of runs at a single composition

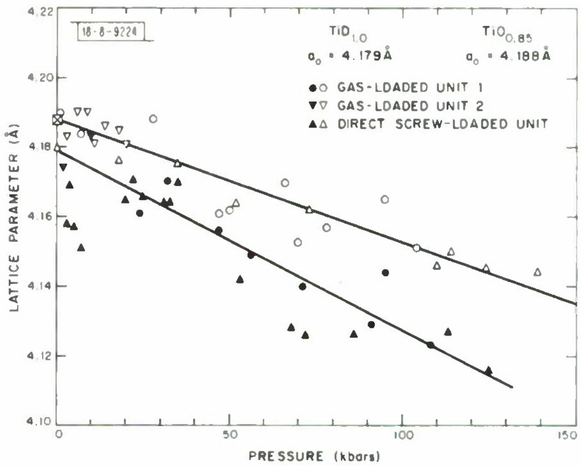

Fig. II-6. Lattice parameter at room temperature versus pressure for cubic $TiO_{0.85}$ and $TiO_{1.0}$.

is made with two or more of the x-ray units, the data are sufficient for a high degree of confidence in the averaged values.

For stoichiometric $TiO_{1.0}$ and the metal-rich $TiO_{0.85}$, the data for lattice parameter as a function of pressure (Fig. II-6) are best represented by straight lines obtained by least-squares analysis of all the data points. Thus, for these compositions, the volume compression does not change significantly from 1 atm to ~140 kbars. The oxygen-rich compositions $TiO_{1.11}$ and $TiO_{1.25}$ exhibit a different behavior, as shown in Fig. II-7. Between 1 atm and 5 kbars, there is a sharp decrease in lattice parameter, corresponding to a large initial volume compression. The compression decreases steadily between 5 and ~20 kbars, above which it becomes essentially constant.

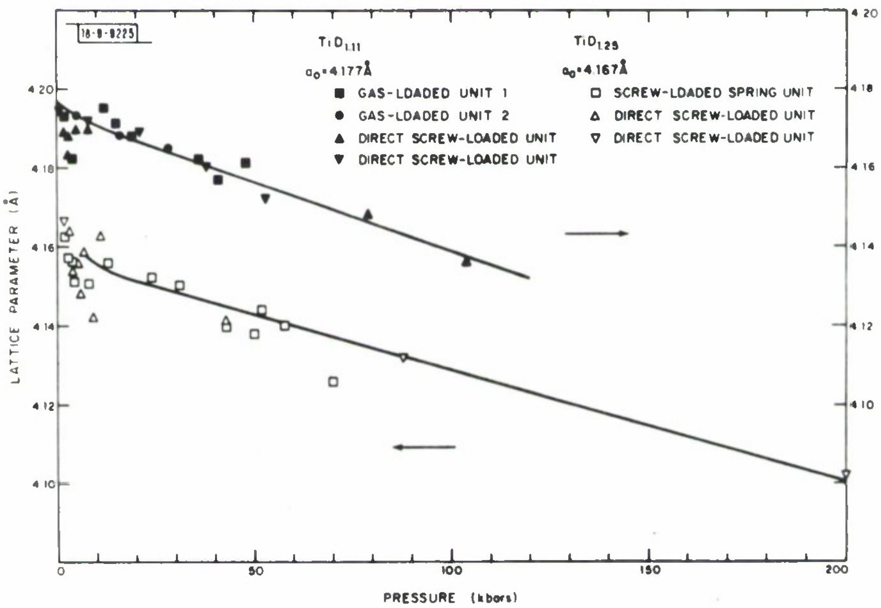

Fig. II-7. Lattice parameter at room temperature versus pressure for cubic $TiO_{1.11}$ and $TiO_{1.25}$.

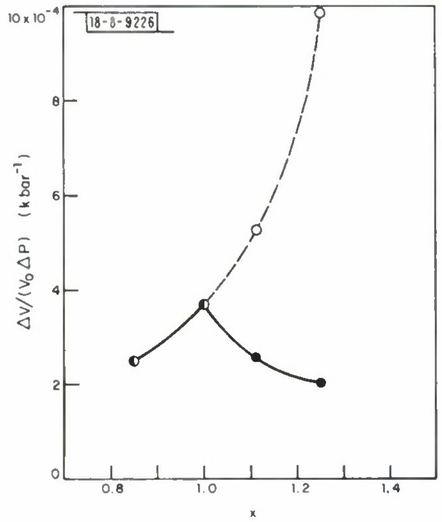

Fig. II-8. Volume compression of TiO_x versus x. Open circles: initial compression (extrapolated to 1 atm). Closed circles: compression at pressures above 20 kbars. Half-closed circles: compression uniform over entire pressure range.

For the four TiO_x compositions investigated, the initial volume compression (between 1 atm and ~5 kbars) increases with increasing oxygen-to-metal ratio (Fig. II-8). Since the total number of vacant lattice sites ($V_{Ti} + V_o$) decreases, from 16 percent of all sites at x = 0.8 to 12 percent at x = 1.25 (Ref. 21), this is an unexpected result. The oxygen ions appear to have a higher initial compression than the titanium ions, since the initial compression increases as the ratio of metal vacancies to oxygen vacancies increases. On the other hand, the volume compression at pressures above 20 kbars (see Table II-3 and Fig. II-8) shows a maximum at the stoichiometric composition, where there are equal numbers of titanium and oxygen vacancies (~15 percent).[21] Because of the higher compression of $TiO_{1.0}$, the molar volume for this composition is less than that for $TiO_{1.11}$ at 50 kbars and less than the volumes of either $TiO_{1.11}$ or $TiO_{1.25}$ above 100 kbars, even though at 1 atm the stoichiometric composition has the largest molar volume of the three.

Possibly the large volume compression of $TiO_{1.0}$ is related to the ease with which this composition is transformed to a vacancy-ordered monoclinic structure by annealing below 800°C. However, $TiO_{1.0}$ does not appear to order under pressure at room temperature, since there

TABLE II-3

VOLUME COMPRESSION OF TiO_x

x	Pressure Range* (kbars)	No. of Runs	$-(\Delta V/V_o \Delta P)$ ($kbar^{-1} \times 10^{-4}$)
0.85	0 to 139	4	2.48
1.00	0 to 125	4	3.68
1.11	20 to 104	7	2.54
1.25	20 to 200	4	2.05

*For linear variation of lattice parameter with pressure.

were no monoclinic lines in the high-pressure x-ray films, including those from the Bassett unit which gave the most detailed patterns. The d-values and lattice constants from such a film taken at 86 kbars with the Bassett unit are listed in Table II-4. The starting material used for these runs was arc-melted $TiO_{1.0}$ which had been splat-cooled in <1 second. No evidence of short or

TABLE II-4

X-RAY PATTERN OF $TiO_{1.0}$ (SPLAT 3) TAKEN AT 86 kbars IN THE BASSETT DIAMOND-ANVIL SQUEEZER (Mo-Kα rad)

(hkℓ)	d-Spacing (Å)	a (Å)
111	2.4097	(Broad line — not used)
200	2.0604	4.121
220	1.4517	4.106
311	1.2454	4.130
222	1.1986	4.152
400	1.0302	4.121
331	0.9460	4.124
		Average 4.126

long range ordering of vacancies was obtained by initial x-ray or electrical measurements on this material at 1 atm. Furthermore, after the pressure runs were complete, the x-ray patterns taken at 1 atm both in the pressure unit and with a standard Debye-Scherrer camera showed no evidence of transformation to the monoclinic structure and gave within experimental error the same a_o value as before the run.

The large initial compression of $TiO_{1.25}$ which we observed does not agree with the results of Iwasaki, et al.[22] They report that the lattice parameter remains constant or even increases slightly between 1 atm and 10 kbars. Above this pressure they obtained $-(\Delta V/V_o \Delta P) = 8.6 \times 10^{-4}\,kbar^{-1}$, four times the value we determined. Since they did not report experimental details other than the use of NH_4Cl as a pressure marker, we cannot comment on this discrepancy. Taylor and Doyle[23] report a value of $5.5(8) \times 10^{-4}\,kbar^{-1}$ for $TiO_{1.0}$, a value 50 percent larger than ours, also without giving experimental details. Based on our experience with diamond-anvil squeezers, a variation of this magnitude is sometimes observed between individual pressure runs on the same sample. The data from several runs must be averaged to obtain reliable results.

M. D. Banus
Mary C. Lavine

REFERENCES

1. Z. Boncheva-Mladenova, A.S. Pashinkin and A.V. Novoselova, Inorg. Mater. 2, 1324 (1966).
2. S.I. Gorboc and A.N. Krestovnikov, Inorg. Mater. 2, 1465 (1966).
3. I.Y. Kashkooli and Z.A. Munir, J. Electrochem. Soc. 117, 248 (1970).
4. G.P. Ustyugov, E.N. Vigdorovich and I.A. Timoshin, Inorg. Mater. 5, 138 (1969).
5. R.F. Brebrick, J. Phys. Chem. Solids 30, 719 (1969).
6. V.M. Glazov, S.N. Chizhevskaya and N.N. Glagoleva, Liquid Semiconductors (Plenum Press, New York, 1969), p. 330.
7. R.F. Porter and C.W. Spencer, J. Chem. Phys. 32, 943 (1960).
8. H.J. Seifert and K. Klatyk, Z. Anorg. Allg. Chem. 342, 1 (1966).
9. J.M. Longo and J.A. Kafalas, J. Solid State Chem. 1, 103 (1969).
10. Y. Syono, S. Akimoto and K. Kohn, J. Phys. Soc. Japan 26, 993 (1969).
11. M. Eibschutz, L. Holmes, H.J. Guggenheim and H.J. Levinstein, J. Appl. Phys. 40, 1312 (1969).
12. G.K. Wertheim, H.J. Guggenheim, H.J. Williams and D.N.F. Buchanan, Phys. Rev. 158, 446 (1967).
13. N. Achiwa, J. Phys. Soc. Japan 27, 561 (1969).
14. J. Portier, A. Tressaud, R. Pauthenet and P. Hagenmuller, C.R. Acad. Sci. Ser. C 267, 1329 (1968).
15. T. McGuire, V.L. Morruzzi and M.W. Shafer, J. Appl. Phys. 41, 956 (1970).
16. N. Menyuk, J.A. Kafalas, K. Dwight and J.B. Goodenough, J. Appl. Phys. 40, 1324 (1969).
17. J.A. Kafalas and J.M. Longo, Mater. Res. Bull. 3, 501 (1968).
18. J.M. Longo and J.A. Kafalas, J. Appl. Phys. 40, 1601 (1969).
19. M.D. Banus and M.C. Lavine, Solid State Research Report, Lincoln Laboratory, M.I.T. (1970:2), p. 42, DDC AD-711074.
20. ______________________, op. cit. (1970:3), p. 26.
21. M.D. Banus and T.B. Reed, Chemistry of Extended Defects in Non-Metallic Solids, L. Eyring and M. O'Keeffe, Eds. (North-Holland Publishing Co., Amsterdam, 1970), p. 488.
22. H. Iwasaki, K. Kamigaki, O. Terasaki and D. Watanabe, J. Phys. Soc. Japan 28, 1095 (1970).
23. A. Taylor and N.J. Doyle, Chemistry of Extended Defects in Non-Metallic Solids, L. Eyring and M. O'Keeffe, Eds. (North-Holland Publishing Co., Amsterdam, 1970), p. 523.

III. PHYSICS OF SOLIDS

A. ELECTRONIC BAND STRUCTURE

1. Shubnikov-deHaas Measurements in $Pb_{1-x}Sn_xSe$

Samples of $Pb_{1-x}Sn_xSe$ with x = 0.08, 0.17, and 0.20 have been studied using the Shubnikov-deHaas oscillatory magnetoresistance effect. Fermi surface shapes and effective masses at the Fermi level have been obtained. In all cases pockets of holes and electrons lie at the L-point on the [111] axis at the Brillouin zone boundary. For the 17 and 20 percent SnSe samples, the Fermi surface is nearly spherical. The anisotropy ratio K (defined as the square of the ratio of the maximum to the minimum cross-sectional area) is 1.0 ± 0.07, while for the 8-percent sample definite anisotropy is seen, corresponding to approximately K = 1.5. For PbSe, a value of K = 2.0 has been reported[1] for a carrier concentration of 6.0×10^{18} holes/cm^3.

The number of carriers deduced from the occupied volume of k-space agrees with Hall measurements ($n = 1/R_He$).

The effective masses obtained from the temperature dependence of the amplitudes of the magnetoresistance oscillations are shown in Table III-1. For comparison the masses were also computed using the two-band model[2] and the six-band result.[3] As in the study of $Pb_{1-x}Sn_xTe$ (Ref. 4), mirror bands were assumed, leaving one undetermined parameter in the two-band case and two in the six-band case. Only the band gap E_g was assumed to vary with composition, x. The values of E_g were taken from the laser emission results.[5] The six-band model, with the two unknown parameters determined by fitting to a pure PbSe sample and to an alloyed sample (H), gives a better agreement with the measured results than the two-band model with one parameter that was determined by fitting to a pure PbSe sample.

J. Melngailis
T. C. Harman
W. C. Kernan

2. Ultrasonic Fermi Surface Studies of Bismuth

Ultrasonic attenuation experiments aimed at exploring the dispersion law for holes in bismuth are under way. Giura, et al.[6,7] reported the disappearance of "giant" quantum oscillations in the ultrasonic attenuation in bismuth for certain angles between the sound wave vector and the magnetic field not quite equal to $\pi/2$. They interpreted this as due to the presence of a saddle point on the hole Fermi surface. If the hole's orbit on the Fermi surface passes through a saddle point in such a way that at some point it has no component of velocity normal to the magnetic field (i.e., the plane of the orbit is tangent to the Fermi surface at a point), Landau quantization breaks down and quantum oscillations should disappear. Presumably the ability of ultrasonic attenuation to see nonextremal Fermi surface cross sections[8] accounts for this breakdown not being observed in other quantum measurements that see only extremal areas (i.e., deHaas-van Alphen and Shubnikov-deHaas effects).

By using ultrasonic frequencies between 20 and 200 MHz, we have explored both the hole and electron Fermi surfaces by means of quantum oscillations. We find very good agreement with

TABLE III-1

EFFECTIVE MASS IN $Pb_{1-x}Sn_xSe$

Sample	x	E_g (eV)	Type	Carrier Concentration (cm^{-3})	A_{111} ($\times 10^{12}$ cm^{-2})	Experimental $\frac{m^*_{111}}{m}$	Calculated $\frac{m^*_{111}}{m}$	
							2-Band	6-Band
Ref. 1	0	0.15	n	Band edge	—	0.040 ± 0.008	0.037 †	0.037 †
A	0.17	−0.035	n	4.7×10^{17}	7.60	0.040 ± 0.004	0.031	0.040
B	0.17	−0.035	n	6.8×10^{17}	8.54	0.044	0.033	0.042
C	0.20	−0.058	n	2.1×10^{17}	4.00	0.035	0.026	0.039
D	0.20	−0.058	n	2.0×10^{18}	16.6	0.062	0.047	0.060
Ref. 1	0	0.15	p	Band edge	—	0.034 ± 0.007	0.037 †	0.037 †
E	0.08	0.045	p	1.6×10^{18}	12.5	0.053 ± 0.004	0.040	0.045
F	0.17	−0.035	p	1.5×10^{17}	4.35	0.030	0.024	0.032
G	0.17	−0.035	p	3.0×10^{17}	5.15	0.033	0.026	0.034
H	0.17	−0.035	p	5.1×10^{17}	7.65	0.040	0.0315	0.040 †
I	0.17	−0.035	p	7.3×10^{17}	9.38	0.047	0.035	0.043
J	0.20	−0.058	p	2.8×10^{18}	20.8	0.068	0.052	0.064

† Fitted.

the effective masses measured by Sakai, et al.[9] By measuring the derivative of the attenuation with respect to magnetic field, we have substantially better signal-to-noise ratio than did Giura, et al., who measured the attenuation directly. We do not see the total disappearance of the oscillations for any angle between q_s and H other than $\pi/2$, but the signal does get rather weak in the neighborhood of the reported disappearance. No explanation has been found for this yet, but the presence of four sheets of the Fermi surface, all giving rise to oscillations of about the same period, suggests a beating between nearly equal periods. Detailed experiments are currently under way to test this hypothesis.

Of perhaps greater significance is the fact that we observe no nonextremal Fermi surface cross sections, even for q_s nearly perpendicular to H (see Fig. III-1). In fact, a careful examination of the data of Giura, et al.,[6] shows that they do not either. This means that the quantum oscillations seen ultrasonically are due to the same Fermi surface cross sections seen in other experiments, and it is no longer obvious why a saddle point should be visible only in an ultrasonic experiment.

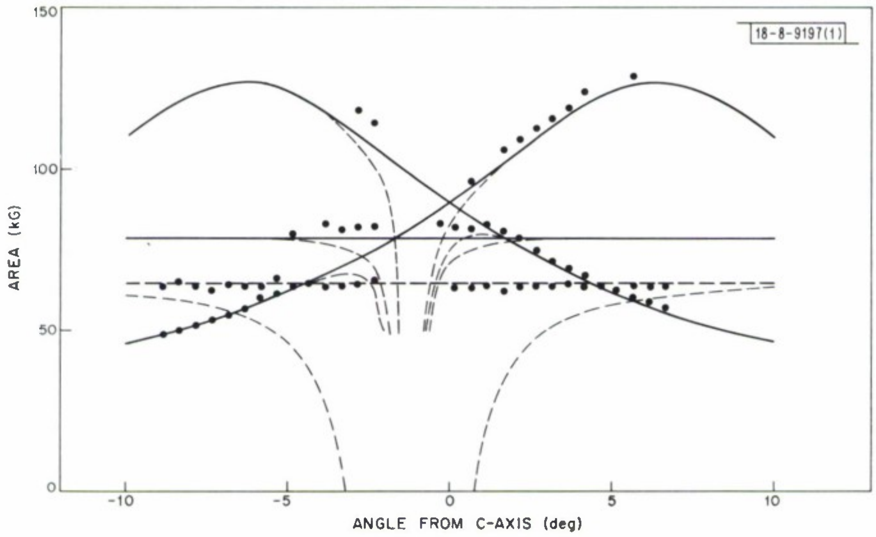

Fig. III-1. Fermi surface cross-sectional area versus angle θ between magnetic field and trigonal axis. Sound is propagated along binary axis. Solid lines are electron extremal cross sections, and broken line is hole extremal cross section. Dashed lines show nonextremal areas that should be observed according to Ref. 8.

Although no nonextremal cross sections are observed, the quantum oscillations still disappear completely (except for geometric resonance) when q_s is exactly perpendicular to H. Since this condition is theoretically linked to the presence of nonextremal orbits,[8] there are some unanswered questions about the nature of the "giant" quantum oscillations themselves. Since $\omega_s\tau$, where τ is the electron lifetime, can be varied easily by using different ultrasonic frequencies, experiments are in progress to study these quantum effects in different scattering regimes. Preliminary results show a broadening of the attenuation peaks as q_s becomes perpendicular to H, but no shift in the period. It is hoped that these measurements will shed some light on the basic processes involved.

V. E. Henrich
B. Feldman

3. Laser Determination of Field Dependent Central Cell Corrections

High resolution, far-infrared laser studies of hydrogenic donors in GaAs have been extended to higher magnetic fields, different transitions and additional samples. For each transition of the hydrogenic model investigated, several extremely narrow lines are observed. Dramatic variations in the relative intensities of these lines are found from sample to sample. Our new results confirm our previous identification[10] that these lines are a consequence of differing central cell shifts of the various donors.

At the high magnetic fields employed in this study, the central cell corrections can no longer be treated as constants. Rather, the nature of the wave function in the immediate vicinity of the impurity and its dependence on magnetic field must be considered. We have accurately determined the magnetic field* dependence of the central cell corrections for the first time. By using perturbation theory, quantitative agreement is obtained with calculations based on effective mass wave functions.[11]

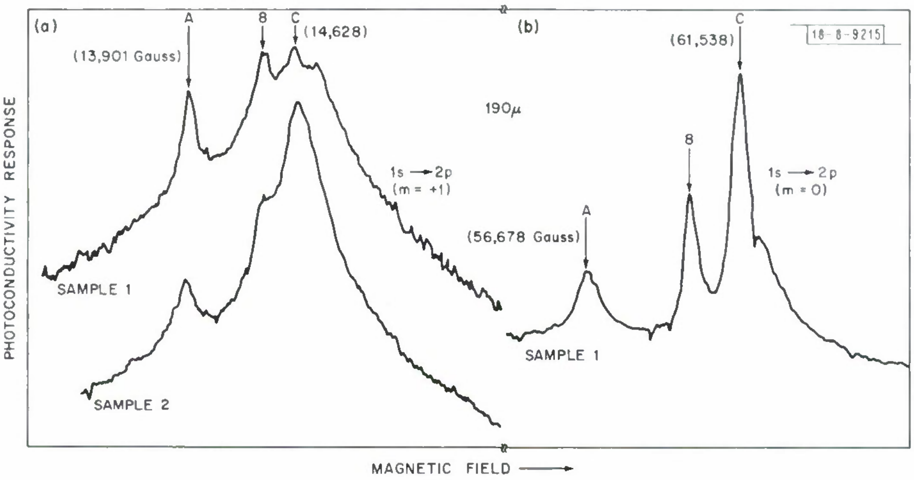

Fig. III-2. Photoconductive signals (bias = 0.5 μa) taken with 190-μ DCN laser as a function of magnetic field: (a) two different samples ($n_1 = 2.0 \times 10^{14} cm^3$ and $n_2 = 4.3 \times 10^{13} cm^{-3}$) showing $1s \rightarrow 2p$ (m = +1) transition; (b) $1s \rightarrow 2p$ (m = 0) transition taken at higher magnetic fields.

Spectra of the 1s to 2p (m = +1) transition, shown for two samples in Fig. III-2, reveal essentially the same donors having different relative concentrations. The B peak, previously detected only by derivative spectroscopy, is now clearly resolved in the sample with the greater impurity concentration. The 1s to 2p (m = 0) transition, shown in Fig. III-2(b), exhibits similar well-resolved structure having a greater dispersion with magnetic field. This is a consequence of the slow variation of the 1s to 2p (m = 0) transition energy in a magnetic field. However, comparison of these measurements with theory requires the data to be converted from transitions at constant laser energy and different magnetic fields to energy separations at constant fields. This was accomplished by two different treatments that yielded good agreement.

---

* Fields up to 100 kG are precisely measured using Al^{27} in a modified Huang NMR oscillator.[12]

In the first method of analysis, a hydrogenic curve was fitted, as a function of magnetic field, to the A peak at all experimental points with an accuracy of better than 0.1 percent. Variations from the hydrogenic model were less than experimental uncertainty, implying small central cell corrections associated with this peak. The energy separations between the A and C peaks at the same fields were then determined from this curve. These results confirmed those obtained by a technique involving no curve fitting. In this second method, the close proximity of several transitions permitted a direct straight-line interpolation from the experimental data. This approach, while limited to the 190- and 195-μ transitions, provided additional verification.

The energies resulting from central cell corrections increase monotonically with increasing magnetic field. Since the deviations from a hydrogenic potential are extremely local,[13] a delta function was chosen to represent the central cell correction. The energy separations, ΔE, between the A and C peaks should then be equal to $\kappa|\psi_s(H)|^2$, where κ is a constant and $\psi_s(H)$ is the magnetic part of the wave function at the origin. Taking normalized hydrogen wave functions, we find $\Delta E/|\psi_s(H)|^2$ and tabulate the results in Table III-2.

TABLE III-2

DETERMINATION OF THE PARAMETER κ AS A FUNCTION OF MAGNETIC FIELD

Wavelength (μ)	Transition 1s → 2p	Magnetic Field Peak Positions (gauss)		ΔE (cm^{-1})	$\kappa = \frac{\Delta E}{\lvert\psi_s(H)\rvert^2}$
		A	C		
195	m = +1	12,960	13,693	1.01	0.0146
190	m = +1	13,901	14,628	1.01	0.0146
119	m = +1	35,922	36,715	1.15	0.0145
195	m = 0	52,043	56,655	1.28	0.0141
190	m = 0	56,678	61,538	1.32	0.0141
78.4	m = +1	65,819	66,806	1.42	0.0148

The good agreement (within experimental error) achieved with this model represents the first observation and confirmation of field dependent central cell corrections. In addition to the theoretical interest of these corrections, it may be possible to use them as an assay technique for electrically active impurity concentrations ranging down to parts per billion.

H. R. Fetterman
J. Waldman
D. M. Larsen
P. E. Tannenwald
G. E. Stillman

4. Semiconductor-Metal Transition in Ti_2O_3

A free energy description of a smooth semiconductor-metal transition has been found which is based on a two-band model and includes electron-electron Coulomb energy and lattice displacement energy. The assumption that the lattice displacement energy plays a weak secondary role leads to good qualitative agreement with a number of experimental observations in Ti_2O_3.

A calculation based on the lattice displacement energy as dominant leads to predictions for the temperature dependence of Raman frequencies in Ti_2O_3 which are inconsistent with experiment.

H. J. Zeiger
T. A. Kaplan*
P. M. Raccah

5. Finite Temperature Conductivity in Half-Filled Band

We have studied the finite temperature, frequency dependent, electrical conductivity for the half-filled band Hubbard Hamiltonian.[14] The conductivity is expanded in inverse powers of the frequency with coefficients given by the frequency-averaged moments. Unlike the infinite temperature moment expansion presented by Ohata and Kubo,[15] at finite temperature each moment contains arbitrarily high powers of the bandwidth, Δ. We are investigating expansions of the low-order moments in Δ, with particular interest in the regime $1 \gg \Delta > kT > \Delta^2/I$; here I is the Coulomb repulsion. Although a direct expansion of the conductivity in Δ requires[16] that the frequency be larger than Δ, an expansion of the moments in Δ does not have this limitation. Our strategy is to find the three lowest moments to order Δ^4 and then use an extrapolation technique[17] to obtain the conductivity at low frequencies.

R. A. Bari
T. A. Kaplan
E. E. Sommerfeldt†

6. Relaxation-Time Ansatz for Quantum Transport Theory: Spin Effects

A relaxation-time Ansatz which treats both orbital and spin relaxation in quantum transport theory has been obtained. For orbital relaxation processes the Ansatz conserves both charge and spin density, and is a modification of a treatment given recently by Green, Lee, Quinn and Rodriguez.[18] The modification is important for treating certain problems involving magnetic fields, in which the spin degree of freedom plays an essential role. In order to treat spin-flip processes, a spin relaxation term is included in an additive fashion in the relaxation-time Ansatz. A general result has been derived for the linear response part of the one-electron density matrix for the case of a space and time-varying perturbation corresponding to a single Fourier component. The results have been applied to calculation of the electrical conductivity, the magnetic susceptibility, and the cross section for inelastic light scattering from semiconductor magnetoplasmas (Sec. III-C-1). A manuscript presenting the theory has been submitted for publication.[19]

R. W. Davies
F. A. Blum

B. MAGNETISM

1. Critique of Standard Procedure for Determination of Paramagnetic Curie Temperatures

The magnetic susceptibility of a ferromagnet above its Curie point T_c is given in the molecular-field approximation by the Curie-Weiss law

$$C/\chi = T - \Theta \quad , \tag{1}$$

* Present address: Physics Department, Michigan State University, East Lansing, Michigan, 48823.

† Summer staff member.

where C is the Curie constant and Θ is the paramagnetic Curie temperature (which equals T_c in the molecular-field approximation). All experiments show nonlinearity of χ^{-1} as a function of T in the neighborhood of T_c, but the curve straightens out at higher temperatures. Furthermore, within the Heisenberg model, Eq. (1) is rigorously valid in the limit of infinite temperature, with the value of Θ proportional to the sum over all the exchange interactions. Consequently Θ is involved in almost all attempts to evaluate these interactions, and is usually obtained by extrapolating the (apparently) linear portion of the χ^{-1} versus T curve back to the temperature axis.

In an early article,[20] Rushbrooke and Wood noted the slowness with which the values of $\chi^{-1}(T)$ calculated from the high-temperature power-series expansion approach their linear Curie-Weiss asymptote. Subsequently Domb and Sykes reiterated this observation and went on to state explicitly that the theoretical asymptote is nowhere near that usually assumed in practice.[21] Since this warning has been almost universally overlooked for various reasons, we choose to rephrase it in even more dramatic terms: Virtually all experimental values for the paramagnetic Curie temperature reported in the literature are significantly in error.

The temperature intercept of a line tangent to the χ^{-1} versus temperature curve is given by

$$\Theta(T) = T - C(T)\,\chi^{-1}(T) \tag{2}$$

with

$$C(T) = 1/(d\chi^{-1}/dT)_T \quad , \tag{3}$$

where T denotes the point of tangency. The Θ and C of Eq. (1) are identical with $\Theta(\infty)$ and $C(\infty)$, respectively. As mentioned above, experimental inverse susceptibility curves appear to become linear, i.e., $(d\chi^{-1}/dT)$ appears to become constant, in the upper portion of the temperature ranges covered. This fact has led experimenters to believe that the molecular-field limit of Eq. (1) has actually been attained and, consequently, to report their measured $\Theta(T)$ as if it were $\Theta(\infty)$.

In order to quantify the resulting errors, we turn to the power-series expansion given by

$$\begin{aligned} T\chi/C &= 1 + \sum_{n=1}^{\infty} a_n (J/kT)^n \\ &= 1 + \sum_{n=1}^{\infty} a'_n (\Theta/T)^n \quad , \end{aligned} \tag{4}$$

where $a'_1 = 1$ and $a'_n = a_n/(a_1)^n$. Then the inverse susceptibility is given by

$$C/T\chi = 1 + \sum_{n=1}^{\infty} b'_n (\Theta/T)^n \quad , \tag{5}$$

where $b'_o = -1$ and

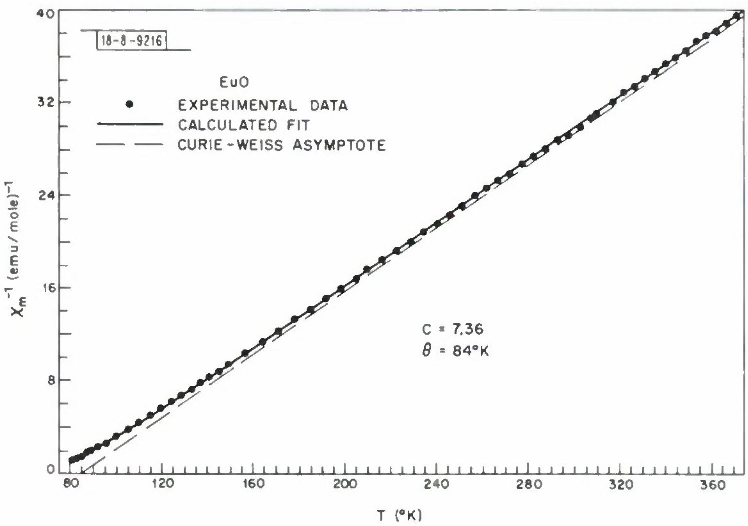

Fig. III-3. Agreement obtained by using high-temperature expansion to fit our experimental inverse susceptibility data for EuO. Solid line represents Curie-Weiss asymptote calculated from power series.

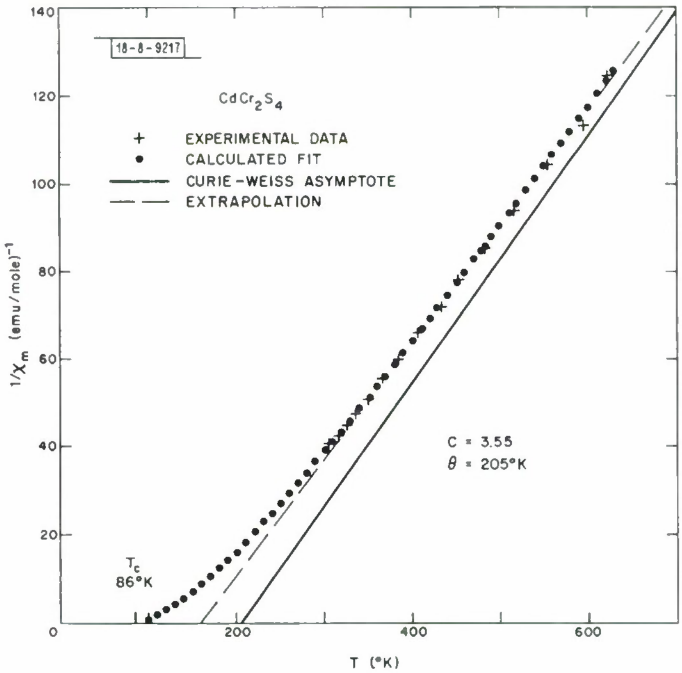

Fig. III-4. Agreement obtained by using high-temperature expansion to fit our experimental inverse susceptibility data for $CdCr_2S_4$. Dashed extrapolation illustrates standard procedure for determining θ; solid line represents true asymptote as computed from power series.

$$b'_n = -\sum_{m=1}^{n} a'_m b'_{n-m} \quad . \tag{6}$$

Straightforward substitutions into Eqs. (2) and (3) yields

$$C(d\chi^{-1}/dT) = 1 - \sum_{n=1}^{\infty} (n-1)\, b'_n(\Theta/T)^n \quad , \tag{7}$$

$$C(T) = C\left\{1 + \sum_{n=1}^{\infty} (n-1)\, b'_n(\Theta/T)^n + \sum_{n,m=1}^{\infty} (m-1)(n-1)\, b'_m b'_n(\Theta/T)^{m+n} \ldots\right\}$$

$$= C\,\{1 + (1 - a'_2)(\Theta/T)^2 + 2(1 - 2a'_2 + a'_3)(\Theta/T)^3 + \ldots\} \quad , \tag{8}$$

$$\Theta(T) = \Theta\left\{-\sum_{n=1}^{\infty} nb'_n(\Theta/T)^{n-1} - \sum_{m,n=1}^{\infty} m(n-1)\, b'_n(\Theta/T)^{m+n-1} \ldots\right\}$$

$$= \Theta\,\{1 - (2 - 2a'_2)(\Theta/T) + (4 - 7a'_2 + 3a'_3)(\Theta/T)^2 - (8 - 20a'_2 + 10a'_3$$

$$+ 6a'^2_2 - 4a'_4)(\Theta/T)^3 + \ldots\} \quad . \tag{9}$$

We see that the leading correction term in the slope is second order in Θ/T, whereas the leading correction to the apparent paramagnetic Curie temperature $\Theta(T)$ is first order. It is for this reason that the slope appears to become constant long before $\Theta(T)$ approaches Θ. Note that the above demonstration did not involve the assumption of any particular model. An expansion for $\chi(T)$ in powers of Θ/T necessarily exists, and its coefficients a'_n can (in principle) be determined from experiment by fitting the observed behavior.

In our study of EuO (Ref. 22), we used such a fitting to determine the constants in a Heisenberg model, but our findings could be presented in an equivalent, model-independent form as: $\Theta = 84°$ K, $a'_2 = 0.937$, $a'_3 = 0.850$, $a'_4 = 0.757$, etc. The high quality of the resulting fit is demonstrated in Fig. III-3. Given the above coefficients, it follows that

$$C(T) = C\,\{1 + 0.063(\Theta/T)^2 - 0.048(\Theta/T)^3 \ldots\} \quad ,$$

$$\Theta(T) = \Theta\,\{1 - 0.126(\Theta/T) - 0.009(\Theta/T)^2 - 0.002(\Theta/T)^3 \ldots \quad .$$

Evaluation at $T = 3\Theta$ and 6Θ shows less than a 0.5-percent variation in $C(T)$, which is a very close approximation to linear behavior, well within experimental uncertainty. Nevertheless, the error in equating Θ with $\Theta(T)$ at $T = 5\Theta$ amounts to 2.5 percent, which is illustrated in Fig. III-3 by the clear separation between $\chi^{-1}(T)$ and its Curie-Weiss asymptote. Such a discrepancy can distort interpretation within the Heisenberg model so seriously as to preclude agreement based on first- and second-neighbor interactions;[22] even the one-percent error anticipated at 1100° K would cause a sizable error in the apparent strengths of the interactions.

A similar fitting process has been carried out for $CdCr_2S_4$. Figure III-4 illustrates the quality of the agreement obtained with $\Theta = 205°$ K, $a'_2 = 0.727$, $a'_3 = 0.395$, $a'_4 = 0.169$, etc. For these coefficients,

$$C(T) = C\{1 + 0.273(\Theta/T)^2 - 0.118(\Theta/T)^3 \ldots\} \quad ,$$

$$\Theta(T) = \Theta\{1 - 0.546(\Theta/T) + 0.096(\Theta/T)^2 + 0.095(\Theta/T)^3 \ldots\} \quad .$$

Our experimental data runs only to $T = 3\Theta$ and its scatter is large enough to mask the 4-percent calculated difference between $C(2\Theta)$ and $C(3\Theta)$. The standard procedure would be to equate Θ with $\Theta(2\Theta)$, as indicated by the dashed line in Fig. III-4, which would yield the enormous error of 24 percent. The error would be greater than 5 percent even at $T = 10\Theta = 2050°$ K.

The above examples demonstrate not only the inadequacy of the usual procedure of measuring some $\Theta(T)$ and calling it Θ, but also the feasibility of using the form of a high-temperature expansion to fit the experimental susceptibility data, Θ being one of the parameters thereby determined. The expansion coefficients need not be those calculated from a particular model; satisfactory results can be obtained by treating the first few a'_n as well as Θ and C as variable parameters, given the measured values of T_c and of the critical exponent γ.[22] We wish to emphasize that some such technique must be used if meaningful values for Θ are to be found.

K. Dwight
N. Menyuk

2. Theory of Temperature Dependence of Two-Magnon Raman Scattering in a Simple Antiferromagnet

We have recently constructed a finite temperature theory for the two-magnon Raman scattering cross section in a simple antiferromagnet. At zero temperature, the results of the theory appear to be in excellent agreement with those one obtains using the two-time Green's function method[23] and the Tyablikov decoupling scheme.

The present theory is based on the finite temperature graphical approach. We employ the Dyson-Maleev transformation to boson operators and reduce the cross-section formula using Wick's theorem for thermal averages. Because spin wave operators were used, the present approach is limited in validity to the temperature range below the critical ordering temperature. Preliminary calculations in this temperature range are now in progress.

R. W. Davies
S. R. Chinn
H. J. Zeiger

3. Raman Scattering in FeF_2

We have observed Raman scattering of argon ion laser radiation in the transparent antiferromagnet FeF_2(T_N = 78.5° K).[24] In addition to the four Raman-active phonons and one- and two-magnon excitations previously reported in the energy range below 500 cm^{-1} (Refs. 25, 26), we see a new series of Raman lines shifted approximately 1100 cm^{-1} from the laser energy. At low temperatures, the most prominent feature is a 30-cm^{-1} broad line with energy ~1090 cm^{-1}, which has an order of magnitude greater intensity than any of the lower energy phonon or magnon lines. From the strength and position of this line, we tentatively identify it as arising from an electronic transition between the A_{1g} and B_{1g} manifolds of the Fe^{2+} ions. Its Raman scattering tensor has B_{1g} symmetry in the D_{4h} space group.

There remain several unanswered questions concerning the detailed identification of this transition. First, the relation of this line to the magnetic dipole absorption observed at 1115 cm^{-1} (Ref. 27) must be made. Second, the most intense line at 1090 cm^{-1} seems to disappear as the temperature is increased to T_N, and higher and lower energy sidebands become more prominent and persist strongly up to 300° K. The exact relation of the 1090 cm^{-1} feature to the magnetic ordering, as well as the correlation between the phonon and magnon energies and the positions of the subsidiary high energy Raman lines, are being investigated. Finally, if possible, spectra will be taken on other FeF_2 samples to examine the possible effects of Fe^{3+} impurities, which may be present in our sample.

S. R. Chinn

C. LASER SCATTERING AND NONLINEAR EFFECTS

1. Light Scattering from Acoustic Plasma Waves and Single-Particle Excitations in Semiconductor Magnetoplasmas

A calculation of the spectra of inelastic light scattering from acoustic plasma waves and single-particle excitations in a one-component, spherical-band semiconductor plasma in a magnetic field has been made. A phenomenological relaxation time Ansatz was used to introduce collisional effects in a cross-section calculation which was given previously. Detailed scattering spectra have been computed as a function of magnetic field using physical parameters appropriate for infrared experiments with conduction electrons in indium antimonide. It was found that screening effects predicted by a simple effective mass theory* were grossly different from those predicted by a more realistic theory which properly treats virtual interband transitions. The general results indicate that the acoustic wave damping in high magnetic fields is sufficiently small and the cross section is sufficiently large to yield an unambiguous spectral identification of this wave with currently available experimental apparatus. A manuscript giving the results of this calculation has been submitted for publication.

F. A. Blum
R. W. Davies

2. Harmonic Generation in Cold Nonuniform Plasma in a Magnetic Field

A variety of recent microwave experiments[29-36] on low-temperature afterglow and cesium electron plasmas in a magnetic field have demonstrated a number of interesting features of both the linear and nonlinear response of the electrons to electromagnetic radiation. The effects studied include reflection,[31] absorption,[32] noise emission,[31,32,36] echo generation,[33-35] and transient "ringing".[29,30] A theoretical discussion[37] of harmonic generation in cold bounded nonuniform magnetoplasmas suggests that harmonic generation experiments may serve as a valuable additional probe of these plasmas. For moderately dense afterglow plasmas, a simple theoretical model[38,39] consisting of a one-dimensional slab of cold nonuniform plasma immersed in a uniform magnetic field (parallel to its faces) has proved capable of predicting the qualitative behavior of both CW linear response[31] and nonlinear echo experiments.[35,39] By means of this theoretical model we have shown[37] (1) that the even harmonic generation is weak compared with the odd harmonic generation, and (2) that strong resonances occur in odd harmonic generation

* Preliminary results based on a simple effective mass theory were given previously.[28]

near cylotron and maximum upper hybrid resonances for small collision frequencies. Observation of the hybrid resonance peak would lend itself readily to plasma density measurement. Measurement of the relative size of even and odd order harmonic generation would serve as an interesting test of the simple cold plasma model. The importance of detailed discharge profile shape and/or thermal effects, both of which have been neglected, might be determined.

F. A. Blum

REFERENCES

1. K.F. Cuff, M.R. Ellett, C.D. Kuglin and L.R. Williams, Proceedings of the International Conference on the Physics of Semiconductors (Dunod, Paris, 1964), p. 677.
2. J.O. Dimmock and G.B. Wright, Phys. Rev. 135, A821 (1964).
3. J.O. Dimmock, Proceedings of Conference on the Physics of Semimetals and Narrow Gap Semiconductors, Dallas, Texas, 20-21 March 1970 (to be published in J. Phys. Chem. Solids Suppl.).
4. J. Melngailis, T.C. Harman, J.G. Mavroides and J.O. Dimmock, Phys. Rev. (to be published, January 1971).
5. T.C. Harman, A.R. Calawa, I. Melngailis and J.O. Dimmock, Appl. Phys. Letters 14, 333 (1969); A.R. Calawa, J.O. Dimmock, T.C. Harman and I. Melngailis, Phys. Rev. Letters 23, 7 (1969).
6. M. Giura, R. Marcon, T. Papa and F. Wanderlingh, Phys. Rev. 179, 645 (1969).
7. M. Giura and R. Marcon, Phys. Rev. B 1, 1528 (1970).
8. V.L. Gurevich, V.G. Skobov and Y.A. Firsov, Soviet Physics JETP 13, 552 (1961).
9. T. Sakai, Y. Matsumoto and S. Mase, J. Phys. Soc. Japan 27, 862 (1969).
10. Solid State Research Report, Lincoln Laboratory, M.I.T. (1970:3), p. 37.
11. D.M. Larsen, J. Phys. Chem. Solids 29, 271 (1968).
12. D.A. Hill and C. Huang, J. Sci. Instr. 43, 581 (1966).
13. W. Kohn, Solid State Phys. 5, 257 (1957).
14. J. Hubbard, Proc. Roy. Soc. (London) A276, 238 (1963).
15. N. Ohata and R. Kubo, J. Phys. Soc. Japan 28, 1402 (1970).
16. R.A. Bari, Phys. Rev. B 2, 2260 (1970).
17. R. Kubo and K. Tomita, J. Phys. Soc. Japan 9, 888 (1954).
18. M.P. Green, H.J. Lee, J.J. Quinn and S. Rodriguez, Phys. Rev. 177, 1019 (1969).
19. R.W. Davies and F.A. Blum (to be published).
20. G.S. Rushbrooke and P.J. Wood, Proc. Phys. Soc. A68, 1161 (1955).
21. C. Domb and M.F. Sykes, Proc. Roy. Soc. (London) A240, 214 (1957).
22. N. Menyuk, K. Dwight and T.B. Reed, Phys. Rev. (to be published).
23. R.J. Elliott and M.F. Thorpe, J. Phys. C, Solid State Physics 2, 1630 (1969).
24. R.C. Ohlmann and M. Tinkham, Phys. Rev. 123, 425 (1961).
25. S.P.S. Porto, P.A. Fleury and T.C. Damen, Phys. Rev. 154, 522 (1967).

26. P.A. Fleury and R. Loudon, Phys. Rev. 166, 514 (1968).

27. J.W. Stout, M.I. Steinfeld and M. Yuzuri, J. Appl. Phys. 34, 1141 (1968).

28. F.A. Blum and R.W. Davies, Solid State Research Report, Lincoln Laboratory, M.I.T. (1970:2), p.58, DDC AD-711074.

29. R.M. Hill, D.E. Kaplan and S.K. Ichiki, Phys. Rev. Letters 19, 154 (1967).

30. D.E. Baldwin, D.M. Henderson and J.L. Hirshfield, Phys. Rev. Letters 20, 314 (1968).

31. F.A. Blum, L.O. Bauer, R.W. Gould and R.L. Stenzel, Phys. Fluids 12, 1018 (1969).

32. R.L. Stenzel and R.W. Gould, Bull. Am. Phys. Soc. 14, 1019 (1969); Rev. Sci. Instr. 40, 1461 (1969).

33. G.F. Herrmann, R.M. Hill and D.E. Kaplan, Phys. Rev. 156, 118 (1967); D.E. Kaplan, R.M. Hill and A.Y. Wong, Phys. Letters 22, 585 (1965).

34. R.W. Harp, R.L. Bruce and F.W. Crawford, J. Appl. Phys. 38, 3385 (1967).

35. L.O. Bauer, F.A. Blum and R.W. Gould, Phys. Rev. Letters 20, 435 (1968); L.O. Bauer and F.A. Blum, Phys. Fluids 13, 2162 (1970).

36. S.J. Tetenbaum and H.N. Bailey, Phys. Rev. Letters 19, 12 (1967).

37. F.A. Blum, to be published.

38. R.W. Gould and F.A. Blum, Eighth International Conference on Phenomena in Ionized Gases (Springer-Verlag, New York, 1967), p. 405.

39. F.A. Blum and L.O. Bauer, Phys. Fluids 13, 2174 (1970).

IV. MICROELECTRONICS

A. GENERAL THIN FILM WORK

Thin film work during this period has involved large numbers of small deposition tasks for various Laboratory programs. A description of several large programs is outlined as follows:

(1) The development of low-temperature coefficient tantalum resistors has been limited because the sputtering unit has been committed to making chromium plates for the mask-making area. However, a new set of masks has been generated, and work is under way to verify previous results and to firm up the parameters involved in sputtering and fabricating low TCR, nitrogen stabilized, Ta resistors.

(2) A technique has been developed for fabricating very high density, air-gap crossovers using 0.005-inch lines and 0.0025 pillars for supporting the beamed crossover. The technique reported by Besseches and Pfahnl of BTL has been modified by replacing the titanium evaporated over the plated copper with a flash of plated gold. Crossovers in excess of 1000 per square inch have been fabricated. Completion of a usable substrate has been delayed by the necessity of acquiring a new mask set. Two of the required masks were contact printed in chromium, but the third had to be rerun on the pattern generator and will be ready shortly.

(3) A technique for fabricating conductive substrates proposed by Mattes (BSTJ, July-August 1970) has been modified to allow fabrication of beam-leaded substrates using flexible, metal foil. In this process an insulator is sputtered (or otherwise deposited) over a metal foil, a conducting layer deposited over the insulator, the circuitry etched in the conducting layer, and the chip apertures etched in the foil and insulator material under the beam regions. Some success has been achieved by sputtering SiO_2 over molybdenum foil and using a Mo/Au conductive film over the SiO_2. The primary problem so far encountered is with pinholes in the insulating layer. However, it seems to be quite feasible to burn out the short circuits resulting from these pinholes. A very attractive application of this type of substrate would be for microstrip circuits. Research in the immediate future will examine the possibility of using photosensitive polymers as the insulating layer replacing sputtered layers. This technique, however, is for general applications and will not be suitable for microwave applications.

(4) In conjunction with Group 86 we have prepared films of various metals on 0211 glass to be used to verify some predictions made by others as to the relationship of metal thickness to neutral density. Each metal

investigated has been evaporated and sputtered to several thicknesses between 200 and 1000 Å. The neutral density will be determined at one or two wavelengths and the thickness of the films accurately determined using both multiple-beam interferometry and the Dektak step-height analyzer. These data will be compared with computer calculated curves of neutral density versus thickness.

(5) Several mounting and interconnection substrates for the photodiode satellite orientation device have been fabricated on disks cut from AlSiMag 772 which is an as-fired 99.6% Al_2O_3 with an 8-microinch surface finish. To insure a better surface for mounting and bonding, these circuits have also been fabricated on 99.5% Al_2O_3 which has been polished on one side to 2 microinches. These highly polished substrates are currently being used to assemble the final units.

(6) Work in conjunction with Group 86 on the preparation of films for the fabrication of surface wave devices by a film parting technique has resulted in the establishment of parameters for substrate preparation and film deposition that results in very high yields on one-of-a-kind substrates. Photoresist patterns which are the negative of the desired circuit are exposed in a positive photoresist applied to the bare substrate, and a duplex film of Ti/Al or Cr/Al evaporated over the photoresist in the electron beam evaporator. The use of the E-beam evaporator is required because of the more nearly point source nature of the evaporation source as opposed to a filament evaporator or, in the worst case, a sputtering unit. The photoresist is then removed and takes with it the excess film. The Cr or Ti is used for additional adhesion.

(7) Considerable effort has been devoted during the past quarter to the preparation of chromium-on-glass masks. A large number of glass plates have been coated with chromium in the sputter-sputter etch module, using a sputter cleaning step before chromium deposition to reduce the number of pinholes to as close to zero as possible. However, this procedure seems to degrade the surface of the glass plates to some degree, and a study of the reciprocal effects of increased pinholes versus superior glass surface will be undertaken. This study will correlate the number of defects (pinholes and chromium-coated defects in the glass) to the sputter etching time and intensity. Considerable work has also been done on the preparation of photoresist coatings, both positive and negative, on chromium-on-glass plates. These plates when exposed have also been developed and etched in the thin film area.

F. J. Bachner

B. GENERAL SEMICONDUCTOR WORK

Several selected semiconductor programs will be described in order to provide a general indication of the overall semiconductor program.

(1) GaAs Schottky barrier millimeter wave diodes have been prepared for the space techniques group. Five-micron diodes on 0.5-mil centers have been fabricated with some units exhibiting series resistance as low as 8 ohms. Two-micron-diameter diodes on 1.0-mil centers have been prepared but difficulties in measuring the devices have allowed only limited evaluation. Apparently one or two diodes exhibit 12 ohms of series resistance which is below worst-case estimates. New masks are in preparation for providing a reduced spacing of diodes to minimize testing and probing problems.

(2) So-called E-Bird semiconductor structures have been prepared with extremely good junctions that are close to theoretical breakdown utilizing a planar structure for reliability. Deep peripheral diffusion gives the high voltage characteristics desired while the 0.5-micron diffusion gives the electron beam amplification desired. The main problem has been the effect of channeling, an increase of surface charges as a result of electron beam irradiation raising the leakage current and thus reducing the breakdown voltage. This appears to have been solved by a thick plating of gold over the sensitive surface oxide, thus masking off the electron beam. Previously only mesa unpassivated diodes were useful in this application at the cost of lowered reliability.

(3) Photodiode arrays (64 diodes per strip) continue to be fabricated for prototype and flight units for the space techniques group. Excellent wafer yield exists but the requirements of 64 consecutively good diodes reduce the overall strip availability on a wafer to perhaps four or five.

R. A. Cohen

C. COMPUTER-AIDED MASK MAKING AND LAYOUT

The mask area began operation in a new area during the past quarter and this period has been devoted to the improvement of techniques and the modification and calibration of equipment in order that the demands placed on the facility by Laboratory programs can be met efficiently and effectively. New personnel are being trained in the use of the mask operating equipment and the quality and quantity of mask production is increasing.

Programming in the mask generation area continues both in advancements and modifications of present programs.

N. B. Childs

D. ENVIRONMENTAL TESTING AND CHIP CLEANING

The environmental test area is now operational. Initially, chambers which provide for extended testing at temperatures above or below room temperature are in service.

Discoloration of aluminum metalization has occurred on some commercial integrated circuit chips during chemical cleaning. This usually is accompanied by pitting of the aluminized surfaces. An investigation of this long standing problem has resulted in a modification of cleaning procedures, particularly with regard to a reduction of the length of time the chips remain in the deionized water rinse.

T. F. Clough

DOCUMENT CONTROL DATA – R&D

(Security classification of title, body of abstract and indexing annotation must be entered when the overall report is classified)

1. ORIGINATING ACTIVITY *(Corporate author)* Lincoln Laboratory, M.I.T.	2a. REPORT SECURITY CLASSIFICATION Unclassified 2b. GROUP None
3. REPORT TITLE Solid State Research	
4. DESCRIPTIVE NOTES *(Type of report and inclusive dates)* Quarterly Technical Summary for 1 August through 31 October 1970	
5. AUTHOR(S) *(Last name, first name, initial)* McWhorter, Alan L.	

6. REPORT DATE	7a. TOTAL NO. OF PAGES	7b. NO. OF REFS
15 November 1970	64	80

8a. CONTRACT OR GRANT NO. F19628-70-C-0230 b. PROJECT NO. 649L c. d.	9a. ORIGINATOR'S REPORT NUMBER(S) Solid State Research (1970:4) 9b. OTHER REPORT NO(S) *(Any other numbers that may be assigned this report)* ESD-TR-70-350
10. AVAILABILITY/LIMITATION NOTICES This document has been approved for public release and sale; its distribution is unlimited.	
11. SUPPLEMENTARY NOTES None	12. SPONSORING MILITARY ACTIVITY Air Force Systems Command, USAF

13. ABSTRACT

This report covers in detail the solid state research work of the Solid State Division at Lincoln Laboratory for the period 1 August through 31 October 1970. The topics covered are Solid State Device Research, Materials Research, Physics of Solids, and Microelectronics. The Microsound work is sponsored by ABMDA and is reported under that program.

14. KEY WORDS

solid state devices	electronic band structure	Raman scattering
materials research	proton bombardment	magneto-optical research
crystal growth	laser scattering	microelectronics
magnetism	infrared	